Spray Cooling on Enhanced Surfaces: A Review of the Progress and Mechanisms

Ruina Xu
Department of Energy and Power Engineering,
Key Laboratory for Thermal Science and Power Engineering of Ministry of Education,
Beijing Key Laboratory for CO_2 Utilization and Reduction Technology,
Tsinghua University,
Beijing 100084, China
e-mail: ruinaxu@tsinghua.edu.cn

Gaoyuan Wang
Department of Energy and Power Engineering,
Key Laboratory for Thermal Science and Power Engineering of Ministry of Education,
Beijing Key Laboratory for CO_2 Utilization and Reduction Technology,
Tsinghua University,
Beijing 100084, China
e-mail: wanggy17@mails.tsinghua.edu.cn

Peixue Jiang[1]
Department of Energy and Power Engineering,
Key Laboratory for Thermal Science and Power Engineering of Ministry of Education,
Beijing Key Laboratory for CO_2 Utilization and Reduction Technology,
Tsinghua University,
Beijing 100084, China
e-mail: jiangpx@tsinghua.edu.cn

The rapid development of high-power electronic, energy, and propulsion systems has led us to the point where the performances of these systems are limited by their cooling capacities. Current electronics can generate heat fluxes up to 10–100 W/cm^2, and heat flux over 1000 W/cm^2 needs to be dissipated with a minimum coolant flow rate in next-generation power electronics. The multiple efficient heat transfer mechanisms have made spray cooling a high heat flux, uniform and efficient cooling technique proven effective in various applications. However, the cooling capacity and efficiency of spray cooling need to be further improved to meet the demands of next-generation ultrahigh-power applications. Engineering of surface properties and structures, which is enabled by state-of-the-art manufacturing techniques, can fundamentally affect the liquid–wall interactions in spray cooling, thus becoming the most promising way to enhance spray cooling. However, the mechanisms of surface-enhanced spray cooling are diverse and ambiguous, causing a lack of clear guiding principles for engineered surface design. Here, the progress in surface engineering-enhanced spray cooling is reviewed for surface structures of millimeter, micrometer, and nanometer scales and hierarchical structured surfaces, and the performances from the reviewed literature are evaluated and compared. The reviewed data show that spray cooling can achieve a critical heat flux (CHF) above 945.7 W/cm^2 and a heat transfer coefficient (HTC) up to 57 W/cm^{2}K on structured surfaces without the assistance of secondary gas flow and a CHF and an HTC up to 1250.1 W/cm^2 and 250 W/cm^{2}K, respectively, on a smooth surface with the assistance of secondary gas flow. A CHF enhancement up to 110% was achieved on a hybrid micro- and nanostructured surface. A clear map of enhancement mechanisms related to the scales of surface structures is proposed, which can help the design of engineered surfaces in spray cooling. Some future concerns are proposed as well. This work helps the understanding and design of engineered surfaces in spray cooling and provides insights for interdisciplinary applications of heat transfer and advanced engineering materials.
[DOI: 10.1115/1.4050046]

1 Introduction

The rapid development of high-power electronic, energy, and propulsion devices [2–4] has led us to the point where the performances of these devices are limited by their heat dissipation capacities [5,6]. Today, the typical heat flux generated by an electronic chip can reach 10–10^2 W/cm^2 [7,8], and in designing next-generation power electronics, it can exceed 1000 W/cm^2 on average at the chip level [9,10] and 1500–5000 W/cm^2 at the hot-spots [3,11], which, if not fully dissipated, results in a temperature rise and a large temperature gradient, causing performance deterioration or even failure of the whole system. Stable and reliable operation of high-power systems requires the cooling system to achieve precise and uniform temperature control, a timely response to a wide range of thermal loads, and reliable startup and long-term stability [3,6,12]. In addition, economic considerations should be taken into account, along with the requirements of high efficiency, miniaturization, and lightweight for the cooling system. Traditional cooling technologies are based on single-phase liquid or air convection, which is limited in heat flux. The thermal loads of current and future electronics are so severe that traditional single-phase convection cooling reaches its limit. Under this circumstance, phase-change cooling, which can utilize the latent heat of evaporation, must be applied [13], as shown in Fig. 1. Among various phase-change cooling methods, namely, pool boiling, microchannel flow boiling, heat pipe cooling, jet impingement cooling, spray cooling, etc., spray cooling has a prominent combination of good cooling capacity, uniformity, fluid utilization efficiency, and system flexibility [2,6,12,14–16]. Along

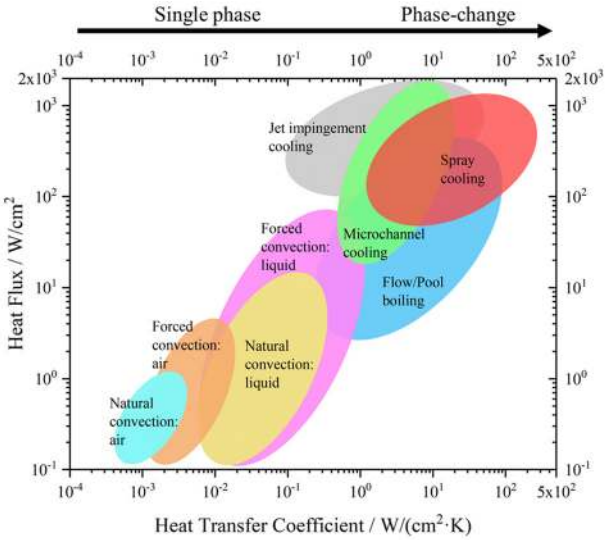

Fig. 1 Comparison of different heat transfer methods

[1]Corresponding author.

Contributed by the Electronic and Photonic Packaging Division of ASME for publication in the Journal of Electronic Packaging. Manuscript received September 22, 2020; final manuscript received January 24, 2021; published online August 6, 2021. Assoc. Editor: Amy Marconnet.

with prominent startup performance and stability, these advantages have brought spray cooling to a wide range of applications, including cooling of supercomputers, space shuttles, drones, hybrid vehicles, lithium-ion batteries, and quenching, as well as next-generation high-power electronic chips, LEDs, lasers and radars [6,10,12,17–21].

In spray cooling systems, a spray of droplets produced by either pressure-atomized or gas-atomized nozzles is forced to impinge onto the targeted heating surface, cooling it efficiently with a phase change of the coolant, as illustrated in Fig. 2. The physical process of spray cooling has multiple advantages that can lead to high cooling performance. The spray droplets can form a uniform and thin liquid film on the hot surface, which evaporates efficiently at the top of the film due to the low thermal resistance through the liquid film [12,22]. The thin liquid film, with a characteristic thickness from tens to hundreds of micrometers to approximately 1 mm [23–27], also enables early and high-frequency breakup of bubbles [28] since bubbles can quickly grow on the film top and rupture. In spray cooling, bubbles can nucleate from either surface nucleation sites due to imperfections, cavities, or secondary nucleation sites created by the impacting droplets via gas entrapment. The spray droplet entrapment, not only benefits nucleate boiling heat transfer but also brings forward the onset of nucleate boiling [29,30]. The momentum brought by the droplets can also accelerate convection in the liquid film [31–33] and the break-up of bubbles [29,34]. In addition, the vapor produced by evaporation can be easily removed through diffusion in a large space or forced convection of the spray stream [35–37], which reduces the vapor partial pressure and enhances evaporation. When the heat flux is approaching the critical heat flux (CHF) in the heating-up direction, the continuous liquid film may degrade to isolated microdroplets that evaporate quickly and efficiently, and heat flux as high as 1000 W/cm^2 and a heat transfer coefficient (HTC) as high as 60 W/cm^{2}K can be achieved [38]. When surface superheats are so high that the vigorous evaporation beneath the droplets creates a vapor cushion, which is known as the Leidenfrost effect, the high-speed droplets can penetrate through the vapor film and delay film boiling and the occurrence of the CHF.

The spray cooling mechanisms ensure that spray cooling has a uniform, efficient, and high cooling performance. On the other hand, to meet the heat dissipation requirements of next-generation power electronics and devices, further development of advanced spray cooling is urgently needed. There are multiple ways to improve the spray cooling performance, including selection and alteration of the working fluid [39–57], optimization of spray parameters [58–62] or systems [17,63–76], and surface engineering. The first two methods are based on the fluid side, which is limited in affecting liquid–wall interactions. Meanwhile, surface engineering of surface chemical compositions, structures, or geometries can significantly influence the surface properties, fluid flow, and heat and mass transfer process at precisely controlled length scales, which enables more possibilities for spray cooling heat transfer enhancement. When a spray droplet is impacting onto a hot, dry surface or a liquid film, it may undergo rebound, deposition, splash, evaporation, nucleate boiling, foaming, transition boiling and film boiling, detailed fluid mechanics of spray droplets can be found in Refs. [77–79]. Nevertheless, all these droplet behaviors are the combined outcomes of different droplet parameters and liquid–wall interactions and can be altered by changing the surface characteristics. Specifically, the characteristic physical lengths in the spray cooling process cover the millimeter, micrometer, and nanometer scales, from nanoscale absorbed liquid film thicknesses of 10–20 nm [80] to microscale triple contact line region thicknesses of 1–3 μm [80], microscale thermal boundary layer thicknesses [81–83], droplet diameters [58,84,85], and bubble diameters [29,86] of tens to hundreds of micrometers, liquid film thicknesses of tens of micrometers to approximately 1 mm [23–27], and millimeter-scale spray areas. The dominant mechanisms may vary for different length scales; thus, changes in the spray cooling process and its heat transfer performance can be achieved by surface engineering across different length scales. In addition, the advancement of micro- and nano-engineering has paved new pathways for the very complicated design and manufacture of enhanced surfaces [87]. The effectiveness of introducing structured surfaces into spray cooling enhancement has been extensively studied and widely accepted [2]. However, the mechanisms of spray cooling enhancement by surface engineering are very diverse and ambiguous, which may cause confuse surface design.

There are two types of application of spray cooling: the first is steady-state cooling of relatively low-temperature targets where surface temperatures are maintained below the critical heat flux limit, and the second type is quenching of a target with a high initial temperature where the target is cooled down gradually. In the case of quenching spray cooling, the cooling starts from the film boiling regime, where spray droplets cannot contact with the substrate due to strong uprising vapor flow. In this review, we mainly focus on steady-state spray cooling, as spray cooling of electronics generally works in low-temperature range and does not involve the film boiling regime or quenching process.

This paper aims to review the progress in surface engineering-enhanced steady-state spray cooling and provide a clear map of mechanisms that can help the design of engineered surfaces in spray cooling. The progress in surface engineering at different length scales is reviewed in detail. The performances, which are critical heat flux, heat transfer coefficient, and cooling efficiency, of the reviewed spray cooling systems are evaluated and compared. The enhancement mechanisms of various structure scales are then discussed and summarized. Some future concerns are proposed as well.

2 Effects of the Characteristic Length Scale of Engineered Structures

As discussed previously, the physical characteristic lengths in the spray cooling process range from the nanometer scale to the millimeter scale and the dominant forces and transport mechanisms may vary on surfaces with different structure length scales. As a result, the spray cooling process and its heat transfer performance can be altered and improved with engineered surfaces,

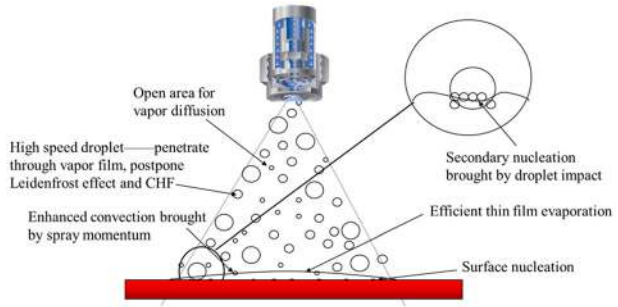

Fig. 2 Schematic of spray cooling mechanisms

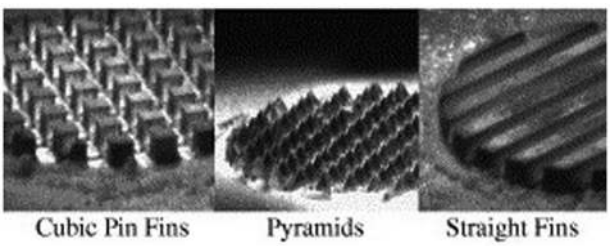

Fig. 3 Millimeter-sized structures. Left: cubic pin fins; middle: pyramids; and right: straight fins (Reproduced with permission from Ref. [88]. Copyright 2006 by IEEE.)

which have been extensively studied. However, for different characteristic length scales, the manufacturing methods are different, and the enhancement mechanisms are diverse and unclear. In this section, recent progress in spray cooling on millimeter-, micrometer-, and nanometer-scale engineered surfaces, and hierarchically structured surfaces is reviewed.

2.1 Millimeter-Scale Structures. Millimeter structures, due to the relatively simple fabrication using traditional machining techniques, were applied in spray cooling heat transfer enhancement in early studies. Typical structures include fins, pin-fins, dimples, etc. that have characteristic lengths of ~1 mm. As described in Sec. 1, the length scales of the thermal boundary layer thickness, droplet diameter, and bubble nucleation are tens to hundreds of micrometers, and the liquid film is on the micro- to millimeter scale, which is within two orders of magnitude difference with the structure scale. As a result, millimeter-scale structures can affect the heat transfer area, liquid flow, and bubble dynamics. In addition to the better simplicity and lower cost of fabrication, millimeter-scale structures can withstand higher temperatures and are more stable than smaller structures because the geometry is less influenced by thermal expansion.

Silk et al. [88] studied PF-5060 spray cooling using a 2×2 nozzle array on three different millimeter-scale-enhanced surfaces directly machined on a heater block, namely, cubic pin fin, pyramid, and straight fin surfaces, as shown in Fig. 3. They found that the straight fin surface enhanced the CHF of perpendicular spray cooling by 58% relative to the flat surface, followed by the cubic pin fin and pyramid surfaces. The enhancement was observed in both the single-phase and multiphase regimes, and the multiphase efficiency was greatly improved from 29% on the flat surface to 46% on the straight fin surface. They suggested that the enhancement resulted from an increased surface area, more nucleation sites, and a longer residence time. They also found that the enhancement did not scale with wetted surface area and suggested that there were other factors, i.e., liquid management on the surface and the utilization efficiency of the wetted area. They also tested more millimeter-sized structures in degassed and gassy conditions [89]. In addition to the structures mentioned above, straight fins with cubic fins on top, dimples, straight fins with dimples, radial fins, and porous tunnels were also studied. The thin straight fin and porous tunnel surfaces showed the highest CHF among the surfaces under both degassed (142 W/cm^2) and gassy (175 W/cm^2) conditions, which were approximately 77% and 62% higher relative to the flat surface under degassed and gassy conditions, respectively. In their subsequent research [90], the geometry of the porous tunnel surface was optimized. Similar structures were also investigated by Wang et al. [91]. Aamir et al. [92,93] also studied air–water quenching spray cooling on the machined straight fin, cubic fin, and pyramid fin surfaces and attributed the observed heat transfer enhancement of structured surfaces to affected bubble dynamics, capillary pumping, and additional liquid circulation. The surface with the sparse pillar array showed a 114.3% higher cooling rate relative to the smooth surface for a starting temperature of 900 °C as a result of the larger nucleation distance and corresponding less intense horizontal coalescence of bubbles, which may trigger the formation of a vapor blanket that could prevent droplet from contacting with the surface. The shape of the pillar could also change the vapor profile.

Xie et al. [94] compared the effect of the fin direction of machined straight fin surfaces in closed-loop R134a spray cooling under 480 kPa. The spray was perpendicular to gravity in a vertically oriented spray chamber, and liquid and vapor were drained from the bottom and top outlets, respectively. Straight fin arrays with a 1 mm width and a 1 mm spacing were manufactured in horizontal and vertical arrangements on the test surfaces. Although the wetted area was enlarged on both surfaces, the vertically arranged surface showed 36% enhanced heat transfer due to the easier drainage of liquid and vapor, whereas the horizontal surface had negative effects on drainage and resulted in a thicker liquid film as well as a higher vapor pressure. Their results showed that the fluid management ability of millimeter-sized structures plays an important role in spray cooling heat transfer.

Under acceleration conditions, the optimum structure may differ from that under normal gravity conditions. Zhang et al. [95] studied water spray cooling under acceleration conditions with machined macrostructured surfaces and found that the surface with drilled holes and a tunnel beneath reduced the surface temperature by up to approximately 40 °C relative to the straight fin surface and a flat surface at the same heat flux. In some conditions, the straight fin surface even had worse heat transfer than the flat surface, again evidencing the importance of the fluid management effect of surface structures.

2.2 Micrometer-Scale Structures. Providing the benefits of millimeter structures, microstructured surfaces are expected to have a stronger influence on spray cooling due to the much denser structures that bring about a larger surface area enhancement. In addition to the strengthening due to the increased number of structures per unit area, reducing the characteristic scale itself increases the importance of the capillary effect and triple contact line evaporation for microstructured surfaces. The most accessible microstructured surfaces are rough (randomly structured) surfaces and porous media-coated surfaces since they widely exist in nature and are easy to manufacture. Meanwhile, the manufacturing of microstructures with precisely controlled geometries is enabled by the advancement of micro-electromechanical systems (MEMS) techniques and has become one of the main methods to enhance phase-change heat transfer. In this section, the progress in applying microstructured surfaces in spray cooling enhancement is reviewed for four types of surface fabrication methods.

2.2.1 Microroughness Surfaces. Flat surfaces with random rough structures can be machined by simple polishing or chemical etching methods. Although not as superior in performance as more complex structures, they are easy, inexpensive, and scalable, thus being promising in large-scale applications. The influence of surface roughness on spray cooling is reviewed in this section.

For pressure-atomized spray cooling, positive effects of increasing surface roughness are widely evidenced by rough surfaces manufactured by polishing with grinding paper [84,96,97], electrical discharge machining (EDM) wire cutting [94], and corrosion or acid cleaning [98,99]. As shown in Fig. 4, Zhang et al. [84] compared pressure-atomized water spray cooling on sand paper-polished surfaces with roughnesses of

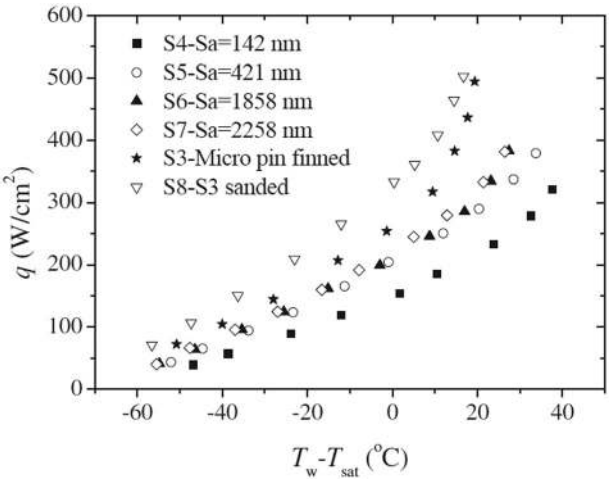

Fig. 4 Effect of surface roughness on spray cooling. Surfaces S4–S7 are flat rough surfaces, S3 is a micropin fin surface, and S8 is S3 polished by sandpaper (Reproduced with permission from Ref. [84]. Copyright 2003 by Elsevier.)

142–2258 nm and found that the heat transfer increased with increasing surface roughness. However, the spray cooling performance on rough surfaces is not as good as that on microstructured surfaces, which will be discussed later. Martínez-Galván et al. [97] clearly summarized that a rough surface could move the onset of nucleate boiling to a lower superheat and extend it along with a wider superheat range. Lee [99] showed that quenching spray cooling heat transfer was better on rough surfaces. It was considered that the surface structure may penetrate through the thermal boundary layer, which is usually approximately 10 μm, enhancing heat transfer. However, a larger surface roughness does not always mean a higher heat transfer. Hsieh et al. [100] compared thin films with roughnesses of 200 nm, 1600 nm, and 50 μm, and it was shown that water spray cooling had the highest CHF on the medium roughness chemical vapor-deposited diamond thin film, followed by the 200 nm roughness sputtered carbon nanotube film and roughest sputtered SiC film coating.

For gas-atomized spray cooling, the trend may be different. Pais et al. [28] studied the influence of surface roughness and its mechanisms on air-atomized spray cooling. A heat flux as high as 1200 W/cm^2 was achieved on the smoothest surfaces with a 0.3 μm roughness. They found that for surfaces with roughness below 1 μm, the dominant heat transfer mechanism was heat conduction through an ultrathin liquid film and evaporation at the liquid–gas interface, which was extremely efficient; however, for rougher surfaces, nucleation heat transfer dominated, and the heat transfer was not as efficient. Their results were in accord with those of Sehmbey et al. [101].

The influence of surface roughness on spray cooling heat transfer differs depending on the spray type and spray cooling regime. For gas-atomized spray cooling, the thin liquid film formed under the force of the gas stream evaporates efficiently and dissipates a high heat flux. In this thin-film evaporation regime, the film thickness and number of nucleation sites would be increased by increasing the surface roughness, which would raise the heat transfer resistance, making the gas-atomized spray cooling perform better on smooth surfaces than on rough ones. However, for pressure-atomized spray cooling, without the assistance of a secondary gas stream, liquid spreading on the surfaces could be enhanced by increasing the surface roughness since the rough surface could reduce the contact angle and provide the additional capillary driving force. Better spreading in spray cooling leads to a thinner liquid film and faster rewetting of dry spots. In addition, without unsaturated gas removing vapor, the thin film evaporation mechanism for pressure-atomized spray cooling is not as dominant as for gas-atomized spray cooling, making the additional nucleation sites brought about by rough surface structures beneficial for heat transfer.

2.2.2 Coated Microporous Structures. Porous media are another type of scalable structure that has random structures covering multiple scales, from millimeter-scale pores to nanopores. The diversity of porous structures enables multiple pathways for spray cooling enhancement, as well as superior fluid management ability. On the other hand, it may introduce extra thermal resistance at the interface between porous media and the base surface. There are two types of microporous structures: one involves the direct coating of a porous layer onto a substrate, and the other involves bonding a premade porous chip onto a substrate. The former has a lower thermal resistance and is reviewed in this section, and the latter is reviewed in Sec. 2.2.3.

One method to coat a microporous layer on a surface is by depositing, evaporating, and sintering a fluid containing microparticles and some carrier or binder substance. Thiagarajan et al. [102] studied HFE-7100 spray cooling on a 100 μm thick microporous copper-coated surface with numerous cavities, as shown in Fig. 5(*a*). The microporous coating was manufactured by screen printing a mixture of silver-coated sub-20 μm copper powder (3 M L-20227) and Dow Corning 704 Diffusion Pump Fluid and subsequent firing in a vacuum furnace. Enhancements of the HTC and CHF relative to plain surfaces as high as 360% and 52%, respectively, were achieved and considered to result from the increased triple contact line density in the porous structure. The onset of boiling was greatly advanced, and the proportion of nucleate boiling was much higher than that on plain surfaces. Kim et al. [103] investigated the effect of a porous coating on air-atomized spray cooling. The microporous coating shown in Fig. 5(*b*) was fabricated by first spraying an mixture of aluminum particles, Devcon brushable ceramic epoxy and methyl-ethyl-ketone (MEK) (ABM mixture) onto a substrate using an Iwata airbrush, followed by evaporating the carrier MEK and leaving a porous layer containing the aluminum particles and binder (Devcon brushable ceramic). The CHF was increased from 1.5 W/cm^2 on the plain surface to 2.1 W/cm^2 at a surface temperature of ~90 °C, and the HTC at 1.5 W/cm^2 was increased by 150% relative to the plain surface. They attributed the heat transfer enhancement to the capillary pumping mechanism, which helped spread and retain the liquid. The study suggested an optimal coating thickness of 100 μm, as a thicker film-induced greater thermal resistance. The particle size, including 8–12 μm, 30–60 μm, and 100–300 μm, had no significant influence on the enhancement. When the particle size decreases, the capillary driving force increases, but this may be offset by the increased flow resistance. Kim et al. [104] studied air-atomized spray cooling on copper surfaces coated uniformly with diamond powder particles with sizes of 6, 13, and 25 μm by the dropping method with a mixture of diamond particle, Omegabond 101 and MEK (DOM mixture). The HTC on microporous surfaces was found to be increased by up to 130% relative to the plain surface. They divided spray cooling on a microporous coated surface into three regimes, namely, complete wetting, evaporative and dryout. In the complete wetting regime, the water supplied was more than that evaporated, and the surface was flooded. In the evaporative regime, the amount of water covering the surface decreased as a result of balance, and the maximum HTC increase occurred in this regime. In the dryout regime, the surface was dry because all the water supplied to the surface was evaporated immediately. They found that a balanced fluid height was a critical heat transfer factor and that variations in the flow rate, particle size, and coating thickness only showed their effects in the evaporative regime by influencing the balanced liquid height. The increase in the HTC on porous structured surfaces due to increased active nucleation sites has also been studied in other works [105–107]. The electroplated microporous coating is also applied in spray cooling. Bostanci et al. [108] studied pressure-atomized R134a and HFO-1234yf spray cooling using the electroplated microporous copper surface shown in Fig. 5(*d*) and found that the HTC and CHF were increased by approximately 25% and 35%, respectively, relative to the plain surface. The enhancement was considered to result from increased nucleate boiling, liquid retention, and spreading caused by the porous structures.

2.2.3 Attached Microporous Structures. The coated microporous structures are not as controllable as premade ones. Silk and Bracken [109] tested the spray cooling heat transfer performance on the commercial metalized porous foam (POCO HTC foam, Entegris, Inc., Billerica, MA) attached to the substrate using two different bonding methods. The foam had an average pore diameter of 350 μm, a total porosity of 61%, a planar conductivity of 70 W/mK, and an out-of-plane conductivity of 245 W/mK. Compared to flat surfaces, the heat transfer on foam-attached surfaces was higher at every flow rate tested, and the CHF was increased by up to 64.6% relative to the flat surface. However, the porous foam created a large thermal resistance along the heat flow path and at the porous foam/base interface, which extensively raised the interface superheat. This negative effect could be partially mitigated through the proper bonding method. Wang et al. [67] studied spray cooling on a surface with superhydrophilic porous copper foam with an average pore diameter of 160 μm attached. They suggested that one of the special advantages of porous surface spray cooling is its application in space environments. The

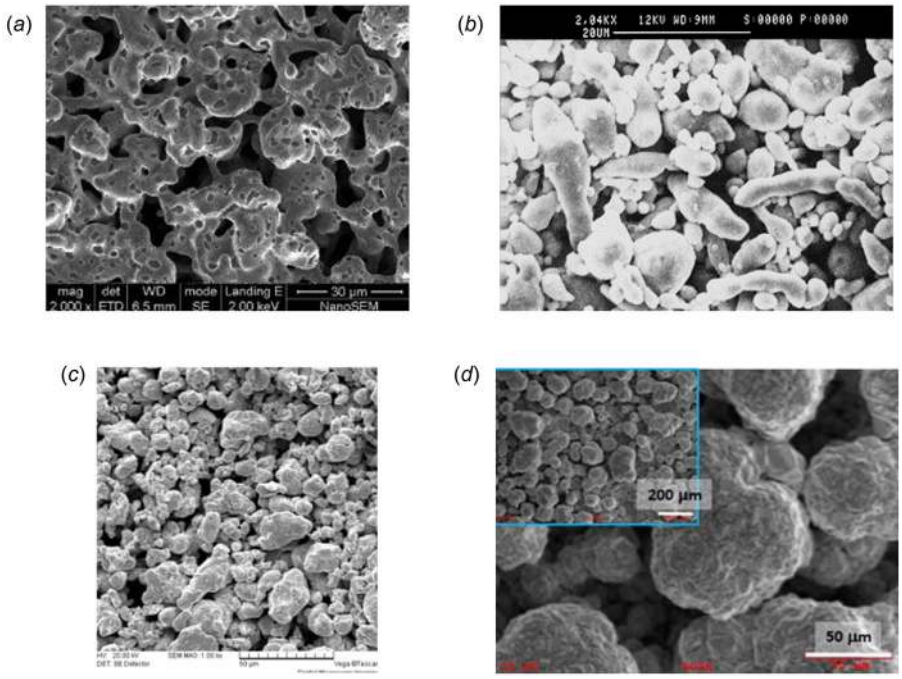

Fig. 5 Images of porous coatings used in spray cooling: (*a*) copper powder coating (Reproduced with permission from Ref. [102]. Copyright 2004 by Elsevier.), (*b*) aluminum particle coating (Reproduced with permission from Ref. [103]. Copyright 2009 by Springer.), (*c*) sintered copper powder coating (Reproduced with permission from Ref. [107]. Copyright 2018 by Elsevier.), and (*d*) electroplated microporous copper (Reproduced with permission from Ref. [108]. Copyright 2010 by American Institute of Aeronautics and Astronautics.)

low gravity condition raises the problem of liquid–vapor separation, which could be solved via the capillary separation of these two phases using a porous coating. However, in their subsequent research [7], the porous surface shown in Fig. 6 was proven to have worse spray cooling heat transfer performance than the flat surface due to the large thermal resistance of 5.02 Km^2/W and weakened droplet impingement on the porous surface. Fortunately, they resolved the problem by covering only half of the flat area with porous foam, simultaneously achieving heat transfer enhancement and liquid–vapor separation.

2.2.4 MEMS-Based Microstructures and Others. Since irregular microstructures can enhance spray cooling heat transfer, it is worth investigating whether precisely designed regular structures can bring about further improvements. Advances in MEMS techniques have enabled spray cooling enhancement through carefully designed surface structures of various scales and geometries.

Hsieh and Yao [110] studied water spray cooling on micropillar arrayed surfaces (with a characteristic size of 120-480 μm, as shown in Fig. 7(*a*)) manufactured by an inductively coupled plasma deep reactive ion etching (DRIE) system. They divided the spray cooling on microstructured surfaces into four different regimes, namely, the flooded, thin-film, partial dryout, and dryout regimes, as illustrated in Fig. 7(*b*). The effect of the micropillars was mainly an increase in the heat transfer in the thin film and partial dryout regimes, and a maximum 17% increase in heat flux in these regimes relative to the plain surface was recorded on the surface with a groove width of 120 μm and a stud size of 160 μm. As evidenced by single droplet impact experiments, the addition of micropillars increased the capillary force, which could reduce the apparent contact angle and enlarge the wetting area, postponing the occurrence of dryout spots and maintaining the high-efficiency thin-film evaporation regime in spray cooling. They also tested these surfaces in a MEMS-based package-level spray cooling system, which was then applied in a personal computer cooling prototype [64]. Spray cooling on micropin fin surfaces was also studied by Chien et al. [111].

Zhang et al. [84,112] also proved the effectiveness of introducing MEMS-based microstructures (with a characteristic size of 25–200 μm) onto spray cooling surfaces and performed massive structure size comparisons, as shown in Fig. 8. They found that the optimal size of microstructures for spray cooling differs for different spray parameters. They also divided spray cooling into four regimes, as illustrated in Fig. 7(*b*), and cooling enhancement was found in the thin film and partial dryout regimes on microstructured surfaces as a result of the increased surface area, capillary wetting ability, and contact line length. The smaller the characteristic size of the microstructures is, the larger the heat transfer area and the better the heat transfer will be; however, if the pillar gap is too narrow or too deep, then the utilization efficiency of the surface area decreases. They measured the mean diameter of the spray droplets and found that the optimal microstructures were those with proper gap width and depth that allowed easy penetration of the spray droplets to the base surface. Chen et al. [87] studied spray

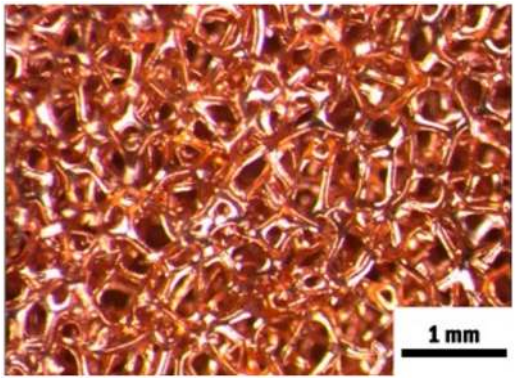

Fig. 6 Superhydrophilic porous copper foam (Reproduced with permission from Ref. [7]. Copyright 2016 by Elsevier.)

cooling on microstructured surfaces using the structures shown in Fig. 9(*a*). As shown by the heat transfer curves in Fig. 9(*b*), the single-phase heat transfer is not enhanced by these structures, although the surface area is enhanced, suggesting that the main enhancement mechanism of these microstructured surfaces is contact line length elongation rather than surface area increase.

Xu et al. [113] studied closed-loop refrigerant R134a spray cooling with DRIE-fabricated smooth, rough, microstructured, and hybrid structured surfaces similar to those studied by Chen et al. [87]. As shown in Fig. 10, the heat transfer was enhanced on microstructured surfaces, and the optimum structure size fit the mean spray droplet diameter, which was 163 μm, suggesting that spray cooling heat transfer could be enhanced the most when the droplet could fit in the gaps between microfins.

Sodtke and Stephan [114] attributed the enhancement of spray cooling on microstructured surfaces (with a characteristic size of 75–450 μm, as shown in Fig. 11(*a*)) to the increased three-phase contact line length on these surfaces. However, the structure fabrication method was not described. The CHF was enhanced from 30 W/cm^2 to 97 W/cm^2 on microstructured surfaces. Through observations with an infrared camera, they found that the contact line length per surface area, as well as, heat flux was enlarged on microstructured surfaces. The temperature gradients near the contact line on a smooth surface were examined using thermochromic liquid crystals and were proven to be larger than those in other areas, making the hypothesis reasonable. Their results validated and extended the triple contact line length enhancement mechanism proposed by Horacek et al. [115,116]. In their following research, it was found that the substrate temperature and heat flux distributions had a local minimum and a local maximum beneath the three-phase contact line, respectively, which is resulted from strong local evaporation.

Coursey et al. [117] studied PF-5060 spray cooling on EDM wire-machined open microchannel surfaces with a channel width of 360 μm, a fin width of 500 μm, and fin lengths of 0.25–5.0 mm. A CHF increase of 36.3%–56.5% was achieved on 3 mm long fin surfaces for various nozzle pressures. The long fins suited the single-phase regime better, while an optimal fin length of 1–3 mm suited the phase-change regime as a result of balance among the increased surface area, varied flow rates, flow channeling effect, and additional thermal conduction resistance. The surfaces were found to advance the onset of phase-change cooling and improve the heat flux and evaporation efficiency through a larger heat transfer area and a longer flow residence time. Hou et al. [118] found that straight fins led to higher heat transfer coefficients than cubic pin fins in the single-phase regime, while in the two-phase regime, the opposite held true, which was reasonable since the stronger confinement effect of straight fins than of cubic pin fins may accelerate fluid in single-phase convection while it may increase the heat transfer resistance in the two-phase regime.

Yang et al. [119] investigated ammonia spray cooling on three microcavity surfaces, as shown in Fig. 11(*b*), and found that the heat transfer enhancement mainly occurred in the high superheat region where nucleate boiling occurred rather than in the low

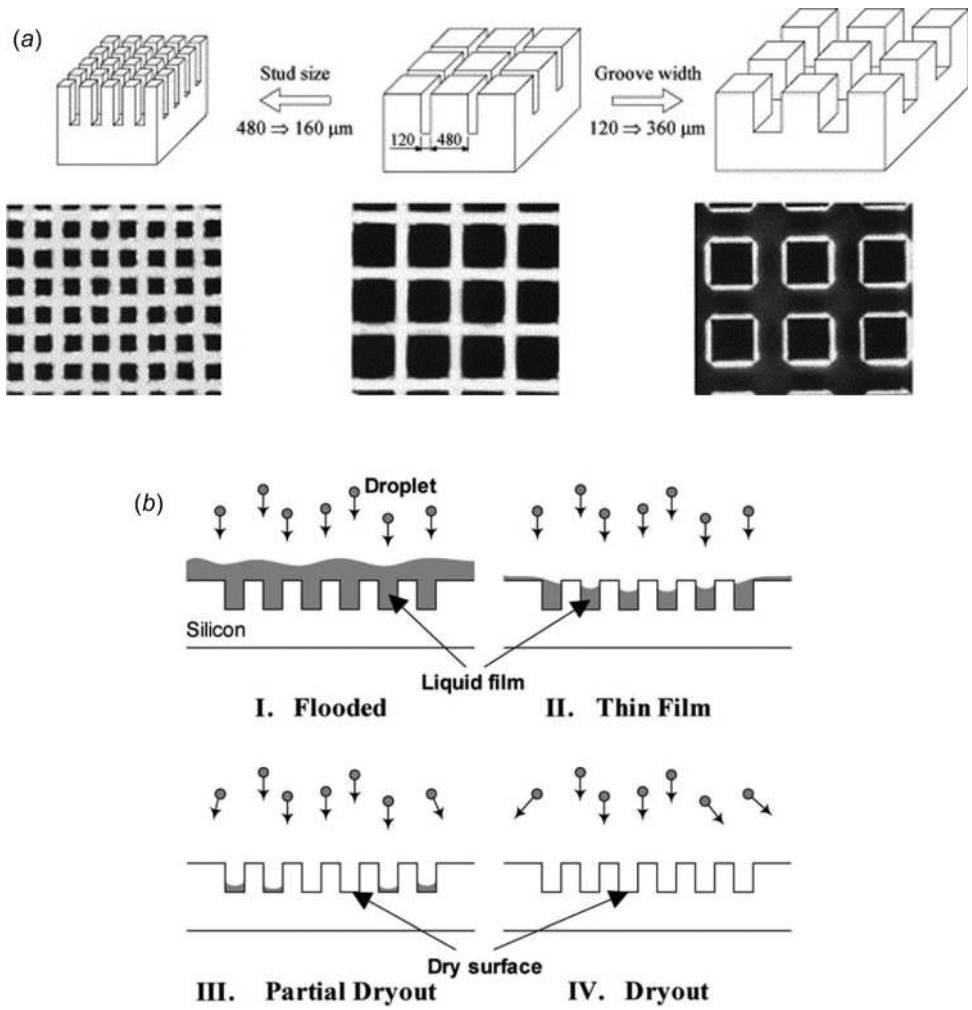

Fig. 7 Spray cooling on microtextured surfaces: (*a*) images of micropin fins and (*b*) schematic of the four heat transfer regimes on the microtextured surfaces (Reproduced with permission from Ref. [110]. Copyright 2011 by Begell House, Inc.)

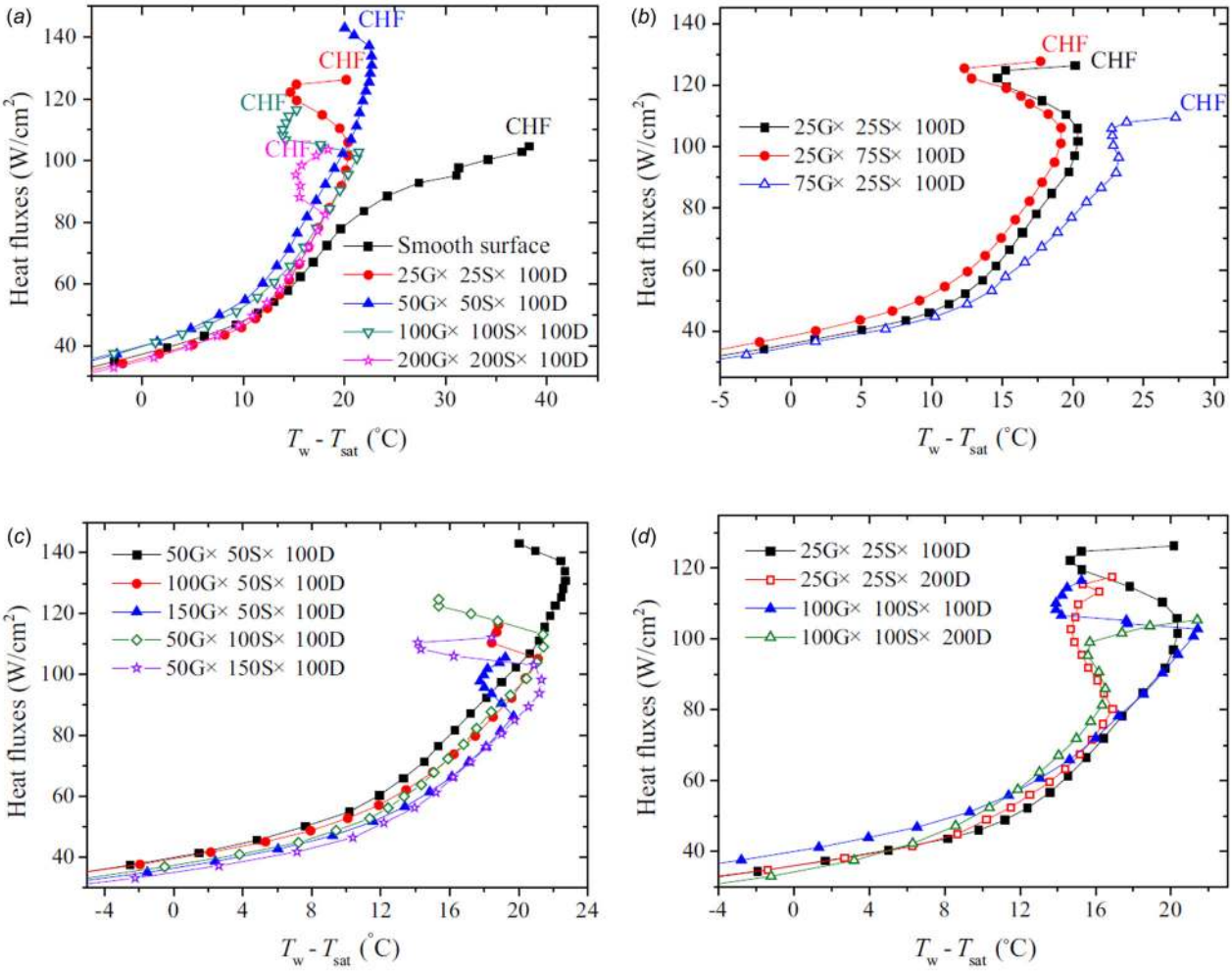

Fig. 8 Effect of micropillar arrayed surfaces on spray cooling (G, S, and D represent the groove width, square stud size, and groove depth, respectively), comparison of different (*a*) 1:1 stud and groove sizes, (*b*) and (*c*) non-1:1 stud and groove sizes, and (*d*) groove depths (Reproduced with permission from Ref. [112]. Copyright 2020 by Elsevier.)

superheat region, which was dominated by single-phase convection. The fabrication method of the structure was not mentioned. The surface with the lowest Bond number ($\mathrm{Bo} = R/\sqrt{\gamma/(\rho_l - \rho_v)g}$) rather than with the largest area enhancement showed the highest heat transfer enhancement, which was a 30% higher HTC at 388 W/cm^2, suggesting that the capillary effect played an important role.

Bostanci et al. [120] performed vapor-atomized ammonia spray cooling on the two types of commercial irregular microstructured surfaces (Rini Technologies, Inc., Oviedo, FL) and found that the HTC at 500 W/cm^2 increased by 112.5% and 50% on the surface with protrusions and roughness of 15–16 μm and on the surface with indentations and roughness of 2–2.5 μm, respectively, relative to that of the smooth surface. The better performance of the first surface was due to the higher surface area and reentrant cavities. HTC hysteresis was observed, that is, a higher HTC was observed in the decreasing heat flux mode than in the increasing heat flux mode, especially on microstructured surfaces, which was due to microcavities retaining vapor and three-phase contact lines.

2.3 Nanometer-Scale Structures. Although nano-engineered surfaces have been extensively studied and proven effective in pool boiling [121–123], the investigations of nano-engineered surfaces for spray cooling enhancement are far from adequate compared to those of millimeter or microstructured surfaces. Nanostructures are much more difficult to fabricate and control than larger structures, which brings about difficulties in the systematic investigation of spray cooling on nano-engineered surfaces. Recent progress [87,124,125] has proven the effectiveness of nano-engineered surfaces. The influence of nanostructures on spray cooling mainly lies in the strengthening of capillary wetting and wicking. Basically, three types of nanomanufacturing techniques are applied in spray cooling research, namely, coated, self-organized, and printed nanostructure fabrication. Moreover, typically, nanostructured layers are very thin, and the extra thermal resistance they introduce into the system can be neglected.

2.3.1 Coated Nanostructures. Zhang et al. [124] studied water spray cooling on surfaces with coatings of one and four layers of carbon nanotubes protected by a plasma-enhanced chemical vapor deposition-deposited 50 nm SiO_2 as shown in Fig. 12. The CHF was increased by 12.6% and 11.6% relative to the smooth surface on the one- and four-layer nanotube-coated surfaces due to the reduced contact angle. Lay et al. [17] applied graphene nanoporous coating to piezo-electric transducer spray cooling of LEDs. The nanoporous coating was manufactured by evaporation and 250 °C curing after a fixed volume of graphene nanoplatelets (GNPs) dispersed in an *n*-butyl acetate solution was applied onto a copper substrate. The nanoporous coating was composed of many hydrophobic graphene layers between which water molecules could move freely without friction, with the oxygenated functional groups in the nanopores providing the driving force, thus making the liquid fully evaporate. Zhou et al. [125] studied

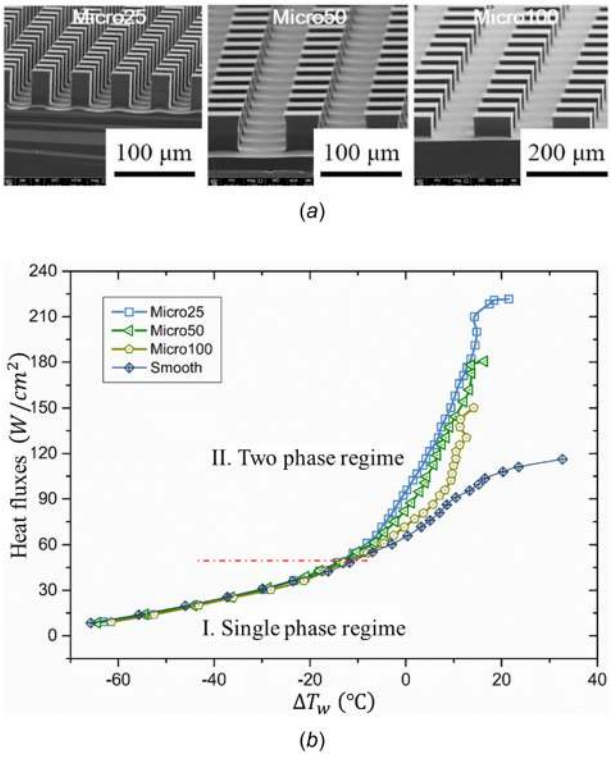

Fig. 9 (*a*) SEM images of MEMS-fabricated micropin fins and (*b*) heat transfer curves of spray cooling on microstructured surfaces (Reproduced with permission from Ref. [87]. Copyright 2006 by Elsevier.)

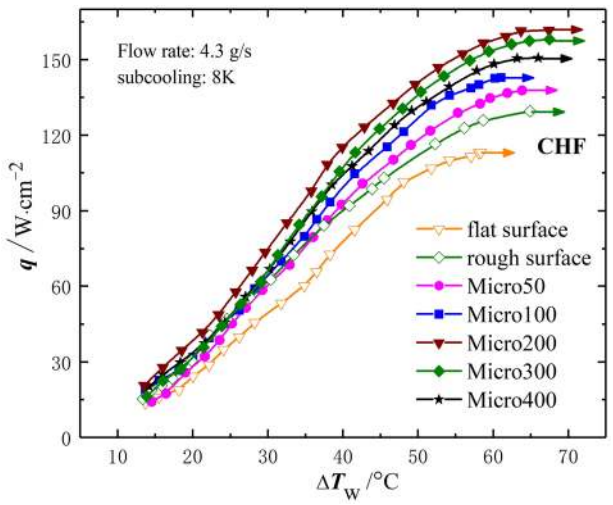

Fig. 10 Heat transfer curves of closed-loop R134a spray cooling on microstructured surfaces (Reproduced with permission from Ref. [113]. Copyright 2007 by Elsevier.)

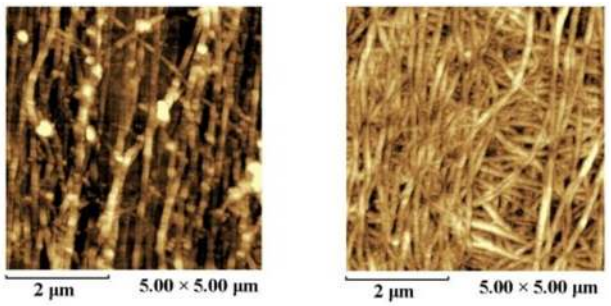

Fig. 12 Images of one (left) and four (right) layers of carbon nanotubes (Reproduced with permission from Ref. [124]. Copyright 2019 by Elsevier.)

R410a spray cooling on nanoporous surfaces with different pore sizes, which were fabricated by depositing nanosilica particles on flat copper substrates by spin coating or electrophoresis using a monodisperse silica solution. An SEM image of a nanoporous surface is shown in Fig. 13(*a*). As shown in Fig. 13(*b*), an HTC as high as 56.92 W/cm^{2}K was achieved on the 30 nm porous surface at a CHF of 222 W/cm^2, which corresponded to a 48% increase in the CHF relative to the smooth surface. The CHFs first decrease and then increase with increasing pore size, which was explained by the existence of "evaporation controlled" and "viscosity controlled" regimes and competition between capillarity and evaporation as spreading driving factors.

Srikar et al. [126] investigated the effect of nanofiber coatings on droplet impingement cooling. It was found that the water-permeable coatings could eliminate droplet receding and bouncing and facilitate full evaporation of droplets. The nanofiber mats could also help retain a thin water film on the surface, accelerating evaporation. As a result, for a substrate at 60 °C, direct impingement of a single water drop could reduce the temperature to 41 °C and 33 °C for the bare substrate and polyacrylonitrile (PAN)-coated substrate, respectively. They tested four types of coatings and found that PAN and poly(methylmethacrylate) nanofiber mats had better thermal stability. In their following research [127,128], they found that the addition of a layer of PAN nanofiber mat coating could enhance the overall heat transfer rate by ~60% and the length of the high heat flux area by ~8% and that it could eliminate the Leidenfrost effect of an ethanol droplet at the substrate temperature of 300 °C and effectively cool it down to 190 °C.

2.3.2 Self-Organized Nanostructures. Chen et al. [18,87] first systematically explored the effect of nanowire arrayed surfaces on spray cooling enhancement and investigated its mechanism experimentally. Regular and irregular ZnO nanowires with various heights were hydrothermally grown on silicon wafers that were predeposited with a zinc seed layer using magnetron sputtering. SEM images of the nanowire arrays are shown in Fig. 14(*a*). The surfaces were superhydrophilic with contact angles as low as 3 deg. They found dramatic increases in the CHF and HTC on nanowire arrayed surfaces. Visualization images showed that the spray droplets formed a continuous film on the nanowire arrayed

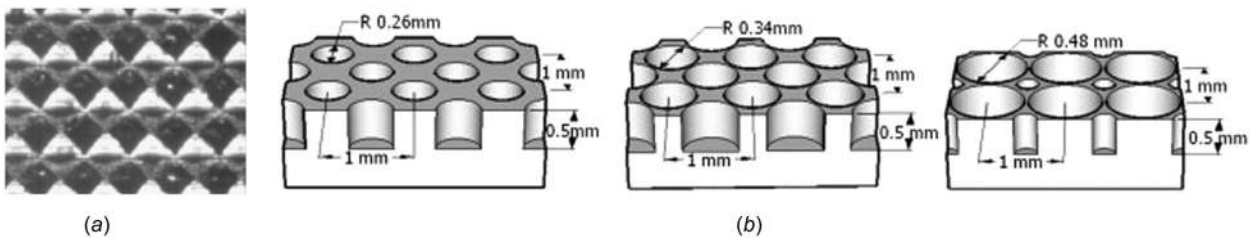

Fig. 11 Images of microstructured surfaces: (*a*) micropyramids (Reproduced with permission from Ref. [114]. Copyright 2005 by Elsevier.) and (*b*) microcylindrical cavities Ref. [119]

surfaces while remaining isolated on smooth surfaces, as shown in Figs. 14(*b*) and 14(*c*). Film rupture did not occur until the superheat was large, after which the heat flux exhibited a steep rise until the majority of the surface area dried out and the CHF occurred. The effects of regular and irregular nanowire arrayed surfaces with various nanowire heights on heat transfer are presented in Figs. 14(*d*) and 14(*e*), respectively. The irregular nanowire arrays outperformed the regular nanowire arrays, and the optimum nanowire height in their study was 9 μm. The CHF was enhanced by 83% to ~220 W/cm^2 on the irregular 9 μm nanowire arrayed surface relative to the smooth surface. Single droplet spreading experiments on nanowire arrayed surfaces were presented in the above paper and discussed in detail in another work [129]. They found that unlike on smooth surfaces where droplets had clear boundaries only at the contact line, droplet spreading on nanowire arrayed surfaces could be divided into the bulk droplet region and wicking-among-nanowires region, as shown in Fig. 14(*f*). The liquid film among the nanowires spread beyond the contact line around the bulk droplet due to the strong capillary effect in the nanostructures, facilitating droplet spreading and evaporation. Considering that the near-zero contact angles on superhydrophilic surfaces are no longer effective for wettability evaluation, they used the dynamic spreading speed to evaluate the wettability of superhydrophilic surfaces. The surfaces with higher spreading speeds showed larger CHF values, as shown in Fig. 14(*g*). They concluded that the superior heat transfer of nanowire arrayed surfaces was the consequence of enhanced spreading of liquid and faster rewetting of dry spots.

2.3.3 Printed Nanostructures. Alvarado and Lin [130] conducted FC-72 single droplet stream cooling on nanostructured surfaces. Surfaces with nanopillars 100 nm high and 200 nm wide were fabricated by the step and flash imprint lithography technique. Infrared thermal images evidenced a more uniform temperature on these surfaces and temperature reductions up to approximately 20 °C relative to flat surfaces under similar heat fluxes. They found that the nanostructured surfaces could lower the film thickness and contact angle by 30% or more, which could benefit heat transfer.

2.4 Hierarchical Structures. Since each structure of different length scales can solely improve spray cooling from different perspectives, it is natural to expect a superior performance by combining different sized structures. It is crucial to construct hierarchical surfaces that combine the advantages of different scales. Basically, hierarchical structures are based on millimeter-scale structures or microstructures, and structures with smaller sizes are added onto these structures.

Millimeter-scale structure-based hierarchical structures are easier to fabricate. Xie et al. [94] studied spray cooling on surfaces with machined millimeter-sized fins with an EDM wire-cut roughness of 3 μm. They found that the performance was better than that of the mere fin surface and mere rough surface, and the maximum heat flux was enhanced by 65% on multiscale surfaces relative to flat surfaces at the same wall superheat. The surfaces combined the merits of a millimeter and microsized structures, namely, surface enlargement, fluid management, and nucleation enhancement. Zhou et al. [125] also studied similar rough millimeter-structured surfaces in an R410a closed-loop spray cooling system and achieved a CHF of 330 W/cm^2, which was 65% higher than that of the smooth surface. Bostanci et al. [131,132] found that multiscale surfaces that had millimeter-sized arrays with roughness below 20 μm achieved a CHF as high as approximately 1,100 W/cm^2 or an HTC as high as 77.2 W/cm^{2}K at 500 W/cm^2 in a vapor-atomized ammonia spray cooling system, which were 19.6% and 161% higher than those of the reference flat surfaces, respectively. The enlarged area and improved fluid confinement played an important role in both cases, while the high CHF was specifically due to the ability of the enhanced surfaces to retain and spread the liquid and thus delay the occurrence of dry spots, and the high HTC was a result of extremely enhanced nucleate boiling. As shown in Fig. 15(*a*), Wang et al. [107] combined macrochannels with a microporous coating in spray cooling, and the HTC on these surfaces was increased by ~166% relative to the flat surface to 16 W/cm^{2}K. The enhancement was considered a result of an enlarged area and an increased nucleation density.

In recent years, hierarchical hybrid micro- and nanostructures have been introduced into spray cooling. Zhang et al. [84] constructed hybrid microstructures by simply polishing a micropin fin surface (characteristic length scale of 150–200 μm) with S36 sand paper, which introduced a roughness of 2.3 μm to the micropin fins. The spray cooling CHF on this hybrid surface was slightly higher than that on the microstructured surface and ~54% higher than that on a surface with a roughness of 142 nm. The HTC at an ~0 °C superheat on the hybrid surface was ~30% higher than that on the microstructured surface and 117% higher than that on the flat surface with a roughness of 142 nm. In their follow-up work [124], microstructures with several layers of carbon nanotubes covering the stud top facilitated a 75.3% increase in the CHF compared to the smooth surface. As shown in Fig. 15(*b*), Chen et al. [87] constructed hierarchical structured surfaces by growing ZnO nanowire arrays on micropin-fin silicon surfaces. As shown in Fig. 16(*a*), the highest CHF on these surfaces was 110% higher than that on the smooth surface, reaching 243 W/cm^2 under a low

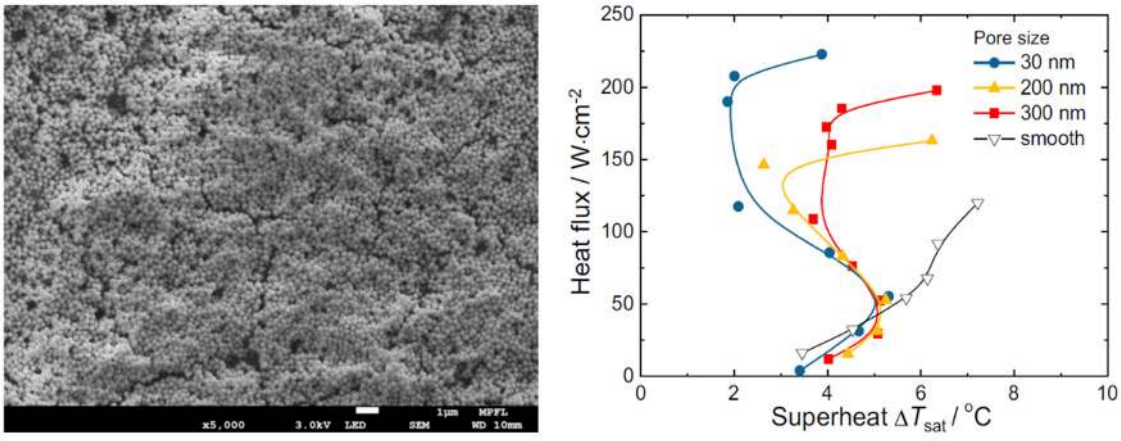

(*a*) (*b*)

Fig. 13 (*a*) SEM image of nanoporous silica and (*b*) heat transfer curves of closed-loop R410a spray cooling on nanoporous surfaces (Reproduced with permission from Ref. [125]. Copyright 2009 by Elsevier.)

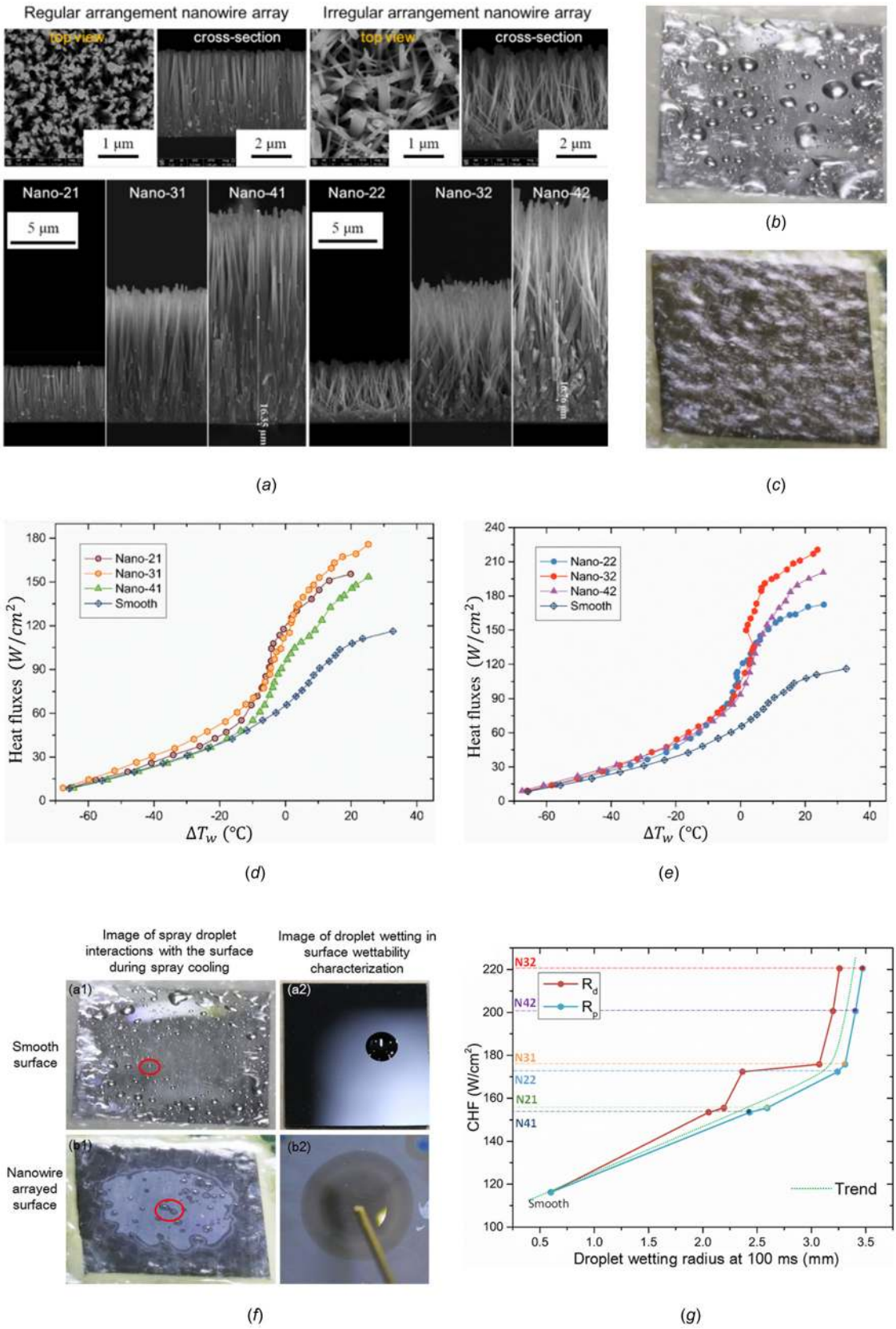

Fig. 14 (*a*) SEM images of regular and irregular ZnO nanowire arrayed surfaces. Liquid distribution in spray cooling on (*b*) a smooth surface and (*c*) a nanowire arrayed surface under a 31.3 W/cm^2 heat flux. Heat transfer curves of (*d*) regular and (*e*) irregular nanowire arrayed surfaces with different nanowire heights. (*f*) Different droplet spreading behaviors on smooth and nanowire arrayed surfaces. (*g*) CHF was proportional to the spreading speed on surfaces (Reproduced with permission from Ref. [18]. Copyright 2009 by IEEE; Reproduced with permission from Ref. [87]. Copyright 2006 by Elsevier.)

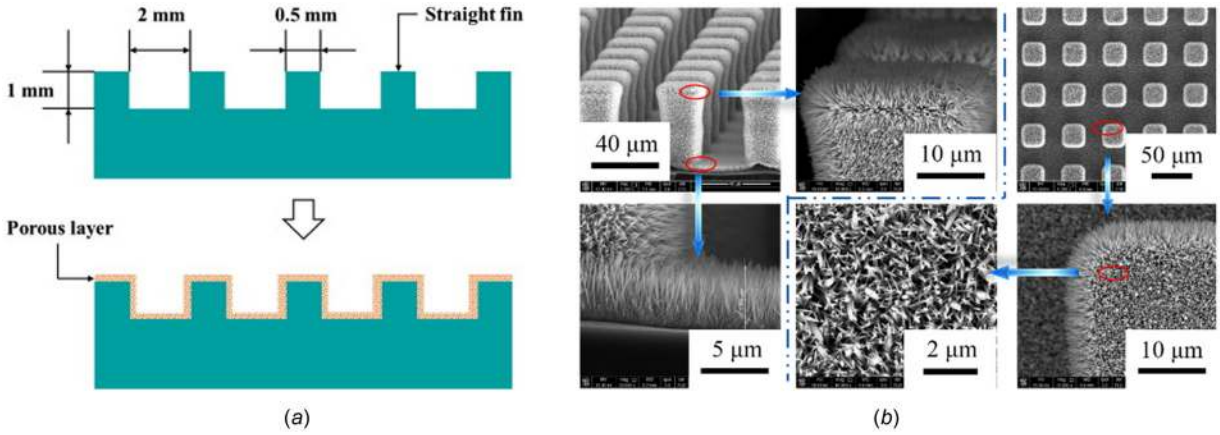

Fig. 15 Hierarchically structured surfaces: (*a*) porous layer-coated millimeter straight fin (Reproduced with permission from Ref. [107]. Copyright 2018 by Elsevier.) and (*b*) SEM images of micro- and nano-structured surfaces fabricated by DRIE and hydrothermal growth of nanowires (Reproduced with permission from Ref. [87]. Copyright 2006 by Elsevier.)

coolant mass flux. The hybrid surfaces outperformed the nanostructured surfaces, and it was found that the 25 μm microstructure outperformed the others. After spray cooling and droplet spreading comparison experiments on these surfaces, they concluded that the hybrid surface combined the channeling effect of the microstructures and wettability enhancement of the nanostructures. Xu et al. [113] studied hybrid micro- and nanostructured surfaces similar to those in Fig. 16(*b*) in a closed-loop refrigerant R134a spray cooling system. As shown in Fig. 16(*b*), compared to the smooth surface, the CHF and HTC were enhanced by 59% to 180 W/cm^2 and 42% to 3 W/cm^{2}K, respectively, and the cooling efficiency was 29.4%. Romashevskiy and Ovchinnicov [133] tested droplet evaporation on direct femtosecond laser processed surfaces that had hierarchical micronanostructures of micropatterns covered with flake-like nanostructures. These superhydrophilic surfaces could significantly accelerate droplet evaporation and increase the Leidenfrost temperature by 30 °C. These surfaces have the potential to be applied in spray cooling.

3 Heat Transfer Performance Comparison

When targeting ultrahigh heat flux cooling, the most crucial evaluation criteria of spray cooling are the CHF, HTC, and cooling efficiency. The critical heat flux (CHF) describes the heat flux limit of spray cooling in the nucleate boiling regime, beyond which the cooling capacity cannot meet the heating rate, causing a rapid increase in surface temperature. At CHF, due to either limited coolant flow rate or the violent bursting bubbles and uprising vapor stream, the coolant reaching the substrate to undergo contact-boiling is peaked. When the flow rate is over-sufficient, at CHF, the surface is flooded with a liquid film accompanied by violent boiling from nucleation [134]. However, when the flow rate is not over-sufficient, droplets may contact the substrate and evaporate separately [87]. The HTC is the heat transfer rate per unit area per Kelvin of wall superheat, which depicts the ability to remove heat flux without much temperature rise of the surface. Imagine a cooling system with a high CHF but a low HTC; although high heat flux can be removed, the surface temperature may rise beyond the operation temperature range. The cooling efficiency, η, of a spray cooling system, as defined in Eq. (1), represents the ratio of the heat flux to the overall sensible and latent heat of the inlet coolant, which describes the ratio of the cooling ability of the supplied coolant that is actually utilized to cool the surface.

$$\eta = \frac{q}{\dot{m}''\left[h_v(T_w) - h_l(T_{in})\right]} \tag{1}$$

where $\dot{m}''$ is the coolant mass flux, $h_v(T_w)$ is the enthalpy of the coolant vapor when it is heated to the wall temperature, and $h_l(T_{\text{in}})$ is the inlet coolant liquid enthalpy.

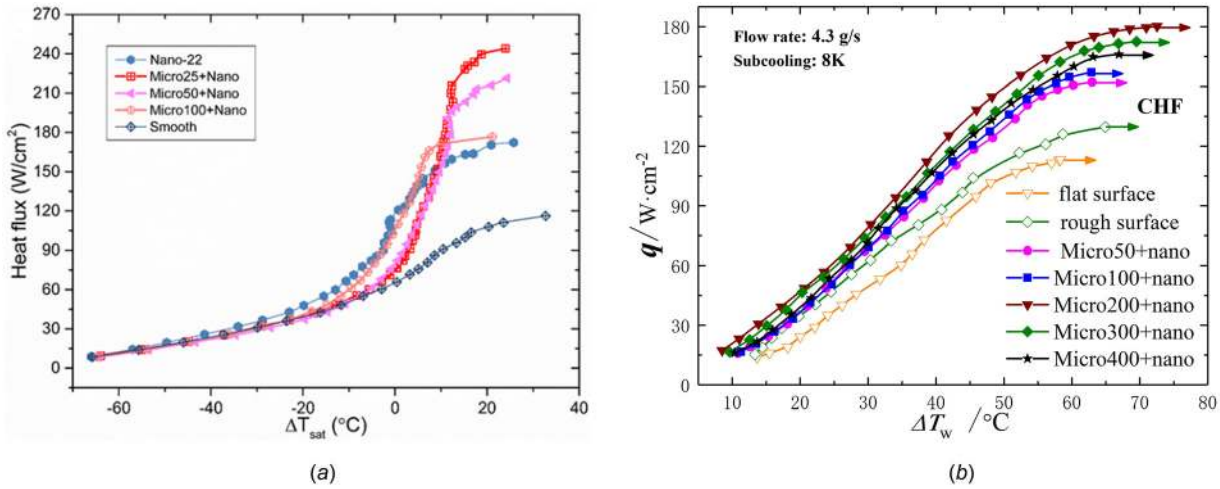

Fig. 16 Spray cooling performance of structures in Fig. 15(*b*) in (*a*) open-loop (Reproduced with permission from Ref. [87]. Copyright 2006 by Elsevier.) and (*b*) closed-loop (Reproduced with permission from Ref. [113]. Copyright 2007 by Elsevier.) systems

Spray cooling data of the reviewed literature are summarized in Table 1, and some data are not exactly precise because they are extracted from figures.

Figure 17 shows the HTC versus CHF data of the reviewed literature. The HTCs of spray cooling lie in the range of 10–100 W/cm^2K, which means that for a heat flux of 10 W/cm^2, the surface superheat can be controlled to below 10–0.1 K. The CHFs of spray cooling can easily reach the range of 10^2–10^3 W/cm^2, which are well beyond current electronic cooling demands and are very likely to meet the next-generation power electronics cooling requirement of over 1,000 W/cm^2 with further development. The highest HTC and CHF are approximately 250W/cm^2K and 1250.1 W/cm^2, respectively, which were achieved by Pais et al. [28] via gas-atomized water spray cooling. However, gas-atomized spray cooling requires extra energy to introduce a secondary gas flow, which can facilitate the removal of vapor and the spreading and thinning of the liquid film. The highest HTC for pressure-atomized spray cooling reviewed is 57W/cm^2K, which was achieved by Zhou et al. [125] with a CHF of 222 W/cm^2 and a wall superheat of 3.9 K in a closed-loop R410a spray

Table 1 Spray cooling data of the reviewed literature

Author, year	Surface type[a]	Working fluid	Spray type[b]	Surface area (cm^2)	Mass flux (kg/m^2s)	CHF (W/cm^2)	HTC (W/cm^2K)	Cooling efficiency η
Ortiz and Gonzalez [96]	Smooth	Water	P	1.23	3.21	155.0	5.96	18.37%
	Smooth	Water	P	1.23	4.10	175.0	6.73	16.24%
	Smooth	Water	P	1.23	6.31	309.0	6.31	18.31%
	Micro	Water	P	1.23	3.21	258.0	6.79	30.30%
	Micro	Water	P	1.23	4.10	322.0	7.16	29.46%
	Micro	Water	P	1.23	6.31	375.0	5.60	21.93%
Chen et al. [59]	Micro	Water	P	1.00	25.60	945.7	25.02	13.95%
Amon et al. [64]	Micro	HFE-7200	P	—	5.53	45.0	1.59	21.93%
Hsieh and Yao [110]	Smooth	Water	P	6.35	0.74	47.5	1.01	23.98%
	Micro	Water	P	6.35	0.74	50.0	0.89	25.08%
Silk et al. [88]	Milli	PF-5060	P	2.00	26.98	140.0	3.54	38.52%
Sodtke and Stephan [114]	Smooth	water	P	3.14	14.15	25.0	4.55	0.71%
	Micro	water	P	3.14	14.15	65.0	10.66	1.85%
Coursey et al. [117]	Micro	PF-5060	P	2.00	14.00	124.0	6.89	70.00%
	Micro	PF-5060	P	2.00	7.98	97.0	2.37	82.00%
Silk [90]	Milli	PF-5060	P	5.14	26.98	141.0	3.53	38.66%
Silk and Bracken [109]	Smooth	PF-5060	P	2.00	28.11	80.0	2.00	19.39%
	Micro	PF-5060	P	2.00	28.11	133.0	1.50	25.91%
Chien et al. [111]	Micro	FC-72	P	1.44	19.27	89.0	3.00	37.60%
de-Souza and Barbosa [105]	Micro	R134a	P	4.91	2.83	40.0	3.88	69.71%
Yang et al. [119]	Smooth	Ammonia	P	3.00	15.00	388.0	10.78	20.77%
	Micro	Ammonia	P	3.00	15.00	451.0	14.84	24.39%
Zhang et al. [84]	Smooth	Water	P	1.13	97.92	675.0	5.87	2.44%
	Micro	Water	P	1.13	97.92	808.0	8.78	2.97%
Xie et al. [94]	Smooth	R134a	P	2.00	41.00	123.0	3.62	13.41%
	Hierarchical	R134a	P	2.00	41.00	270.7	5.88	28.11%
Martinez-Galvan et al. [97]	Micro	R134a	P	1.61	63.25	190.0	8.44	14.73%
de-Souza and Barbosa [106]	Smooth	R134a	P	4.91	1.70	28.0	1.27	77.11%
	Micro	R134a	P	4.91	1.70	29.0	3.22	84.76%
Thiagarajan et al [102]	Smooth	HFE-7100	P	1.00	224.04	105.0	3.00	3.01%
	Micro	HFE-7100	P	1.00	224.04	189.0	10.50	6.27%
Zhang et al. [112]	Smooth	Water	P	0.55	0.78	100.4	2.94	48.30%
	Micro	Water	P	0.55	0.78	145.0	7.25	70.50%
Wang et al. [67]	Micro	Water	P	2.00	22.50	245.0	5.57	4.06%
Zhang et al. [124]	Smooth	Water	P	0.55	1.24	123.7	4.40	37.63%
	Hierarchical	Water	P	0.55	1.24	216.9	12.19	66.51%
Zhang et al. [95]	Smooth	water	P	1.96	2.57	150.0	3.33	22.07%
	Milli	water	P	1.96	2.57	150.0	15.00	22.67%
Wang et al. [107]	Smooth	ammonia	P	3.00	10.56	313.0	6.66	22.73%
	Hierarchical	ammonia	P	3.00	10.56	350.0	16.67	26.57%
Bostanci et al. [108]	Smooth	R134a	P	1.00	42.63	240.0	4.53	24.23%
	Micro	R134a	P	1.00	54.81	370.0	5.95	27.96%
Wang et al. [7]	Smooth	water	P	2.00	25.20	400.0	16.00	6.01%
	Hierarchical	water	P	2.00	25.20	470.9	21.40	7.09%
Chen et al. [87]	Smooth	water	P	1.44	1.24	119.0	3.66	36.08%
	Hierarchical	water	P	1.44	1.24	243.0	9.72	74.10%
Zhou et al. [125]	Smooth	R410a	P	1.77	37.91	200.0	5.33	24.81%
	nano	R410a	P	1.77	37.91	222.0	56.92	32.33%
	Hierarchical	R410a	P	1.77	37.91	330.0	18.64	44.77%
Pais et al. [28]	Smooth	water	G	1.00	13.58	1250.1	250.02	35.91%
Sehmbey et al. [101]	Smooth	water	G	0.81	6.57	750.0	8.33	41.29%
Bostanci et al. [131]	Smooth	ammonia	G	2.00	10.05	780.0	18.14	57.65%
	Hierarchical	ammonia	G	2.00	13.20	1090.0	20.19	60.20%
	Hierarchical	ammonia	G	2.00	10.05	910.0	19.78	66.90%
Bostanci et al. [132]	Smooth	ammonia	G	2.00	10.05	500.0	29.41	38.82%
	Hierarchical	ammonia	G	2.00	10.05	500.0	80.65	39.70%

[a]Surface type: "milli" stands for millimeter scale structured surfaces.
[b]Spray type: p-pressure-atomized spray and g-gas-atomized spray.

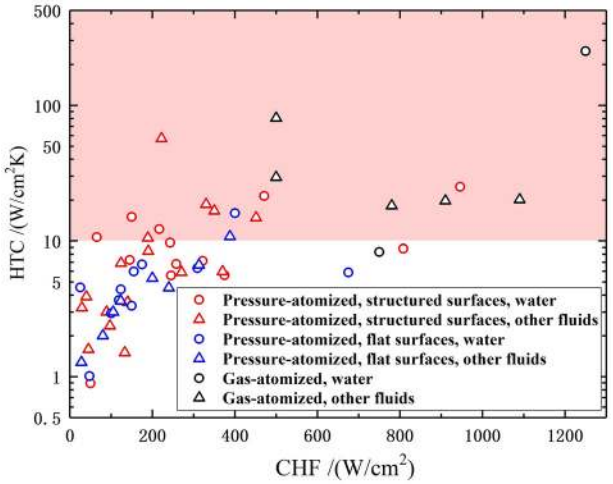

Fig. 17 CHF and corresponding HTC results of the reviewed literature

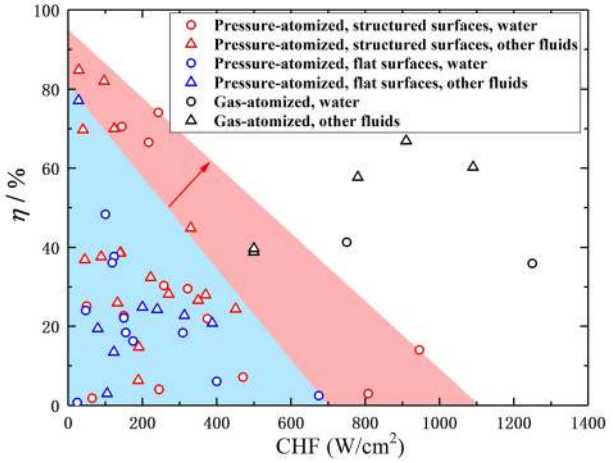

Fig. 19 CHF and corresponding cooling efficiency results of the reviewed literature

cooling system with an enhanced surface. The highest CHF for pressure-atomized spray cooling reviewed is 945.7 W/cm^2, with which the HTC was as high as 25W/cm^{2}K [59]. As highlighted in Fig. 17 by the pink background, most pressure-atomized spray cooling results with HTCs above 10W/cm^{2}K are based on structured surfaces, showing the effectiveness of surface structures.

Generally, the CHF increases with coolant mass flux since more cool fluid can be heated and vaporized. In Fig. 18, the cooling efficiency versus mass flux data is presented. When the coolant mass flux is very small, the cooling efficiency is usually close to 100% because once a coolant droplet is sprayed onto a hot surface, it can be immediately vaporized. However, when the coolant mass flux is increased, the cooling efficiency decreases. This downward trend results from the increased thermal resistance and reduced liquid residence time at a large flow rate and causes waste of coolant at high CHFs. Therefore, to overcome this drawback, one of the objectives of improving the spray cooling performance is to increase the CHF and cooling efficiency at the same time.

Figure 19 summarizes the CHF and corresponding cooling efficiency results of the literature reviewed in this paper. As shown in Fig. 19, the performance frontier of pressure-atomized spray cooling on flat surfaces is extended by structured surfaces, which demonstrates the significant effects of surface engineering as a spray cooling enhancement method. In addition, due to the secondary gas flow, with moderate coolant mass fluxes, the cooling efficiency and CHF of gas-atomized spray cooling are better than those of pressure-atomized spray cooling, as shown in Figs. 18 and 19. Moreover, as shown in Figs. 18 and 19, nonwater fluids have higher cooling efficiencies than water at the same flow rate, but their CHFs are not significantly higher than that of water because their latent heats of vaporization are much smaller than that of water.

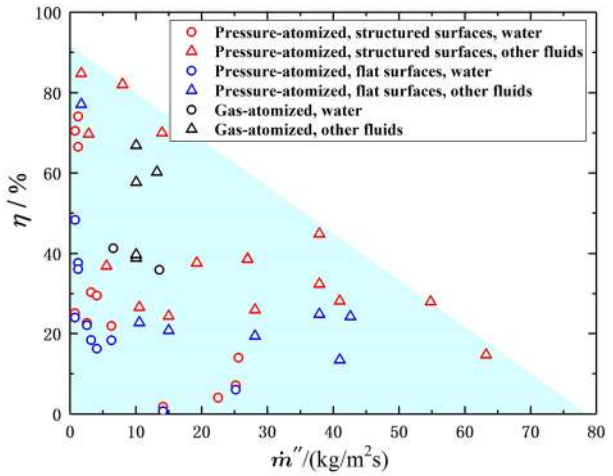

Fig. 18 Downward trend of cooling efficiency η with increasing $\dot{m}''$ based on literature data

4 Enhancement Mechanisms of Surface Engineering

As described in Sec. 2, there are multiple pathways through which surface structures can affect the spray cooling process. First, the contact angle can affect spray cooling heat transfer regardless of the surface structure. Second, the structures can affect heat transfer by influencing the heat transfer area, nucleate boiling behavior, triple contact line length, confinement of fluid, and wickability. The relative importance of different pathways varies with the structure scale since the relevant mechanisms are sensitive to the characteristic length scales and number density of structures. In this section, the scale effects of different mechanisms are analyzed.

4.1 Effects of Contact Angle Variation. The contact angle is a critical factor for spray cooling since it can affect both liquid spreading and bubble formation. Surfaces with different chemical compositions have different contact angles even if they are identical in geometry because the chemical composition can directly

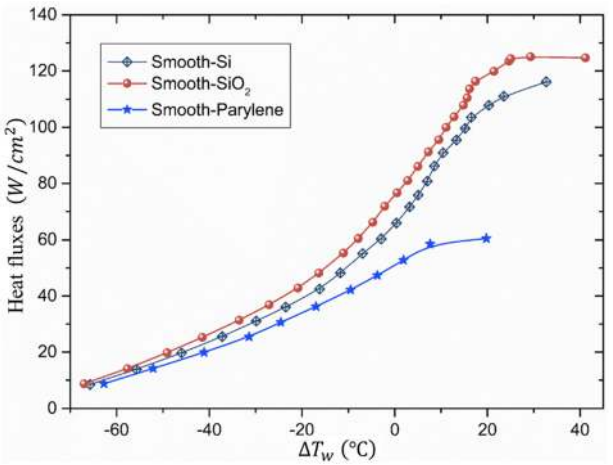

Fig. 20 Effect of contact angle on spray cooling heat transfer (contact angles (CAs): Si-54 deg, SiO_2-32 deg, parylene-115 deg) (Reproduced with permission from Ref. [18]. Copyright 2009 by IEEE.)

Fig. 21 Images of liquid distribution in spray cooling on a (*a*) SiO_2-coated surface, CA = 32 deg, (*b*) silicon surface, CA = 54 deg, and (*c*) parylene-coated surface, CA = 115 deg (Reproduced with permission from Ref. [18]. Copyright 2009 by IEEE.)

affect the liquid-wall adhesion force. Additionally, the effects of contact angle are diverse for different spray types.

In pressure-atomized spray cooling, a low contact angle assists the spreading of liquid film and rewetting of dry spots, which can increase the spray cooling heat transfer. Chen et al. [18] compared spray cooling on chemically altered smooth silicon surfaces (Ra roughness < 2 nm) with contact angles of 32 deg (SiO_2 coated), 54 deg (bare silicon), and 115 deg (parylene coated). The CHF and HTC increased with decreasing contact angle, as shown in Fig. 20. Visualization measurements showed that a large area of the liquid film was formed on the hydrophilic surfaces, while isolated droplet islands existed on the hydrophobic surface, as shown in Fig. 21. The delayed occurrence of the CHF on the hydrophilic surfaces may be attributed to the elevated Leidenfrost temperature due to the better hydrophilicity [135].

In gas-atomized spray cooling, a thin film that can wet the whole surface is easily formed by the shear strength of the gas flow. Sehmbey et al. [101] studied air-atomized spray cooling on smooth copper, nickel, and gold surfaces with contact angles of 47 deg, 48 deg, and 63 deg and found that surfaces with larger contact angles showed higher HTCs because they can enhance nucleation and help provide stable surface-adhering bubbles that can grow to an optimum size, thus enhancing boiling heat transfer.

4.2 Heat Transfer Area Enlargement. One of the determinants of total heat transfer is the effective heat transfer area, which can be increased by surface structures. Intuitively, the denser and smaller the structures are, the larger the total surface area is and the better the heat transfer is. While this may be true, the thickness of the thermal boundary layer should also be considered. As illustrated in Fig. 22(*a*), heat is transferred mainly through conduction in the thermal boundary layer with thickness δ_T [136]; thus, the heat flow Q across the surface can be estimated by

$$Q = \frac{\lambda_l (T_w - T_\infty) A_{\mathrm{TBL}}}{\delta_T} \tag{2}$$

where λ_l is the thermal conductivity of the liquid and A_{TBL} is the area of the thermal boundary layer. When the surface structures are not immersed by the liquid film, as shown in Fig. 22(*b*), only a proper structure gap that fits the diameter of the droplets can enhance the contact area between the droplet and microstructures and increase the heat transfer area [112]. In most cases, a liquid film exists on the surface. When the structure sizes are larger than the thermal boundary layer thickness, the structure enlarges the area of the thermal boundary layer A_{TBL}, as illustrated in Fig. 22(*c*). When the sizes of the structures are much smaller than the thermal boundary layer thickness, the shape and area of the thermal boundary layer are not significantly changed by these structures, as illustrated in Fig. 22(*d*). For nucleate boiling, the thermal boundary can be estimated as $3.22\lambda_l/h$ [81], where h is the heat transfer coefficient. For water at 150 °C and an h of

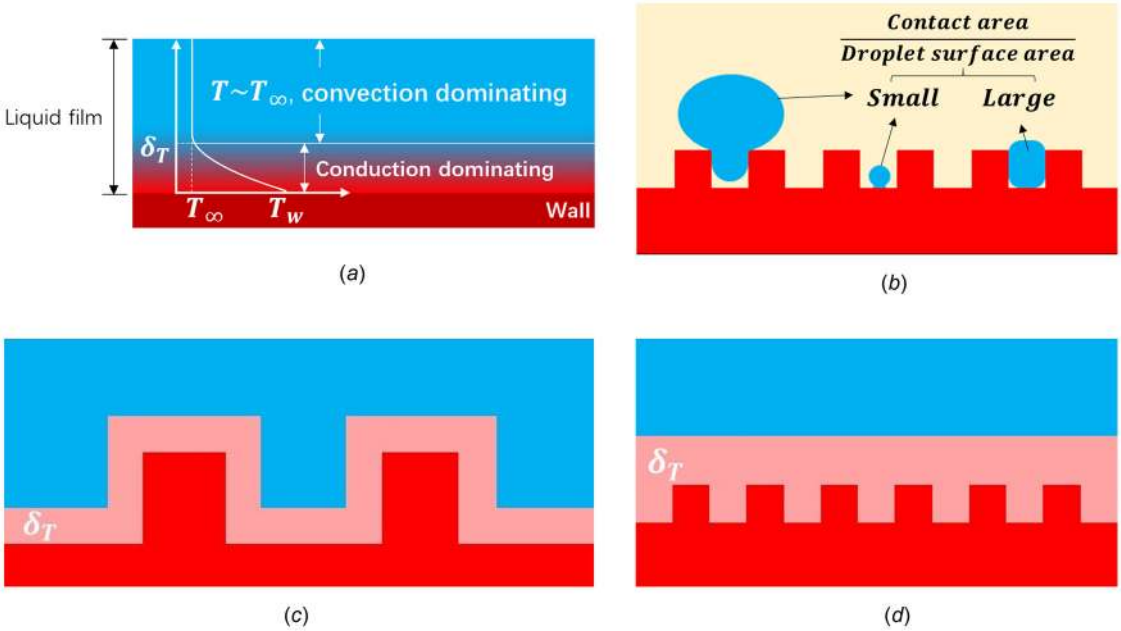

Fig. 22 Illustration of (*a*) thermal boundary layer, (*b*) surface area enhancement of dropwise evaporation on structured surfaces; surface area enhancement effect for (*c*) large structures, and (*d*) small structures

5 W/cm^{2}K, the thermal boundary layer thickness is ~44 μm. Sometimes the thermal boundary layer thickness can be as high as hundreds of micrometers [82]. Thus, surface area enhancement is one of the main enhancement mechanisms for millimeter-scale structures. For microstructured surfaces, the increase in surface area is not as important when the structures are immersed by the thermal boundary layer in the liquid film.

4.3 Nucleate Boiling Enhancement. Although nucleate boiling is the dominant heat transfer mechanism in pool boiling, it only occurs in spray cooling when the liquid film thickness surpasses a critical value [137]. When the liquid film is thin enough for the thermal boundary layer to reach the film top, evaporation at the film top is a more efficient and preferred phase-change process than nucleate boiling because of the lower vapor diffusion resistance and absence of bubble growth resistance. However, when nucleate boiling does occur in spray cooling, it can also enhance heat transfer through not only a phase change but also disturbance of the liquid film and creation of a triple contact line by rupturing the film. It is worth mention that the growth of a bubble inside a droplet can also lead to a second spreading of the droplet, causing an enlarged heat transfer area and increased evaporation rate [138]. Nucleate boiling can be enhanced by increasing the nucleation site density through surface engineering. As illustrated in Fig. 23, vapor bubbles can nucleate at surface cavities with a proper mouth radius.

According to heterogeneous nucleation theory [86], the range of active nucleation cavity sizes is controlled by the thermal boundary layer thickness and the combination of the Clausius–Clapeyron and Young–Laplace equations. For cavity sizes that are too small, the bubble embryo requires higher equilibrium heat than supplied, while for oversized cavities, the top of the bubble is beyond the thermal boundary layer, causing condensation and hindering further growth. The range of active cavity sizes can be predicted by the following equation:

$$\left\{ \begin{matrix} r_{c,\max} \\ r_{c,\min} \end{matrix} \right\} = \frac{\delta_T}{4}\left[1 - \frac{\theta_{\text{sat}}}{\theta_w}\left\{ \begin{matrix} + \\ - \end{matrix} \right\}\sqrt{\left(1 - \frac{\theta_{\text{sat}}}{\theta_w}\right)^2 - \frac{12.8\sigma T_{\text{sat}}(P_l)}{\rho_v h_{fg}\delta_t \theta_w}}\right] \tag{3}$$

where $r_{c,\max}$ and $r_{c,\min}$ are the upper and lower bounds of the active cavity size, respectively, δ_T is the thermal boundary layer thickness, $T_{\text{sat}}(P_l)$ is the saturation temperature of the liquid at a pressure of P_l, ρ_v is the vapor density, $\theta_{\text{sat}} = T_{\text{sat}}(P_l) - T_\infty$ and $\theta_w = T_w - T_\infty$, where T_∞ is the ambient temperature and T_w is the wall temperature.

According to Eq. (3), for saturated water at atmospheric pressure, the ranges of active cavity sizes for $\delta_T = 10$, 100, and 1000 μm are plotted in Fig. 24. Cavities with mouth sizes of 1–10 μm are most likely to be activated, and those of tens to hundreds of micrometers are likely to be activated with thicker thermal boundary layers. Therefore, for a surface with microcavities, nucleate boiling can be significantly enhanced in spray cooling, while millimeter-sized structures only enhance nucleation in certain circumstances due to the lower active nucleation site density. It is worth mentioning that in addition to the bubbles nucleated from surface cavities, the secondary bubbles entrapped by impacting droplets can also facilitate nucleate boiling [29,139–142], which is one of the unique mechanisms of spray cooling.

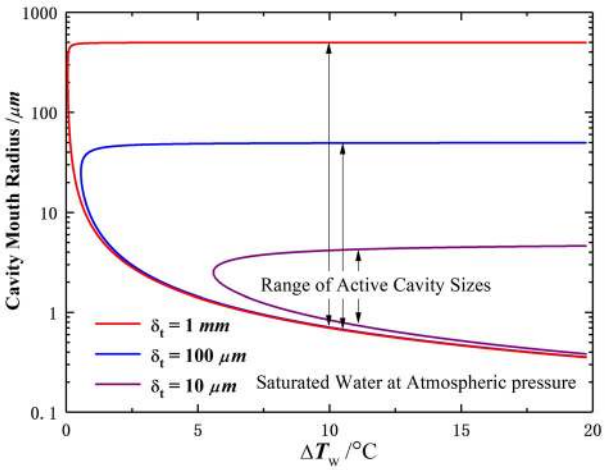

Fig. 24 Range of active cavity sizes for various thermal boundary layer thicknesses and varying wall superheat

4.4 Triple Contact Line Elongation. One of the most important spray cooling mechanisms lies in the three-phase contact line region. The contact line region, defined as the transition region between the dry surface or ultrathin absorbed film and the bulk droplet, as shown in Fig. 25, has been extensively studied and widely accepted as a preferred region for evaporation to occur [143]. This region has a varying thickness of only 1–3 μm and a width of 0.5 to 10–20 μm [80]. This region experiences low thermal conduction resistance between the liquid–vapor and liquid–solid interfaces, which provides adequate heat supply, sufficient liquid supply from the bulk droplet, and low vapor diffusion resistance above the region. Furthermore, molecules are constrained near the wall by short-range van-der-Waals forces in the ultrathin absorbed film region while the forces have no significant influence on evaporation at the liquid–vapor interface in the contact line and bulk region [138,144]. As a consequence, vigorous evaporation continuously occurs in the contact line region, creating a heat flux up to an order of magnitude higher than the average flux across the droplet [80]. Ibrahem et al. [145] found that the substrate temperature and heat flux distributions had a local minimum and a local maximum beneath the three-phase contact line, respectively, which is resulted from strong local evaporation. They found that the heat flux at the contact line is 5.4–6.5 times higher than the average heat flux across the heating region. Specifically, the most vigorous evaporation lies in the

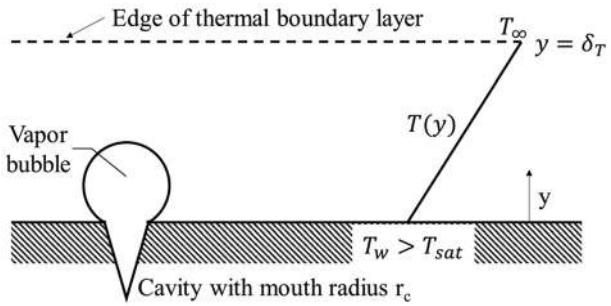

Fig. 23 Illustration of heterogeneous nucleation at surface cavities

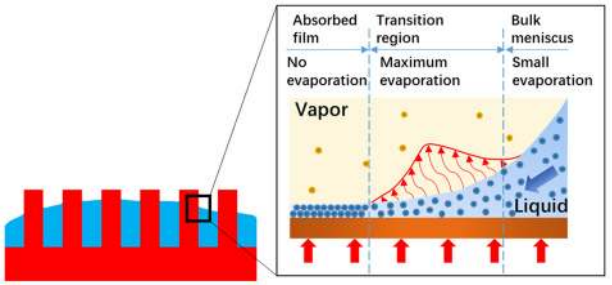

Fig. 25 Illustration of the triple contact line elongation effect and contact line structure and physics

submicrometer-thick transition region between the absorbed layer and the bulk meniscus, where the disjoining pressure and capillary pressure are equally important [146]. Putnam et al. [38] studied microdroplet evaporation and found that the contact line length per unit surface area was the most critical factor to maximize the heat flux and heat transfer coefficient in spray cooling, which can be achieved by simply spraying microdroplets onto microstructured surfaces. Based on their study, spray cooling in the dropwise evaporation regime can yield a heat flux of over 1000 W/cm^2 and an HTC of over 60 W/cm^{2}K. On a smooth surface, the triple contact line region only exists when the film is ruptured, which limits the spray cooling heat transfer, whereas on macro- or microstructured surfaces, the thin liquid film shape and heat transfer are significantly different from those on a smooth surface due to puncture of the liquid film caused by the structures, and the triple contact line length is greatly enlarged, which was visually measured by Sodtke and Stephan [114]. This enables the earlier dominance of the ultrafast triple contact line evaporation mechanism under a lower wall superheat. Since the thicknesses of the liquid film (tens to hundreds of micrometers) and contact line region (1–3 μm) and the width of the contact line region (0.5 to 10–20 μm) are all within the microscale, both macro- and microstructures can extend the triple contact line length. In particular, with denser structures, more triple contact lines can be created on microstructured surfaces than on macrostructured surfaces, making the extension of the triple contact line one of the dominant mechanisms for microstructured surfaces.

4.5 Flow Confinement. In addition to the mechanisms summarized above, surface structures may also enhance spray cooling by flow confinement and redistribution, as illustrated in Fig. 26. The liquid film, with a thickness of approximately 10–1000 μm, flows across the surface with confinement by the micro- or macrostructures, which benefits heat transfer in multiple ways. First, with space being occupied by the structures, the liquid must spread to a larger area, creating a larger heat transfer area. Second, due to the conservation of mass flux, the fluid may speed up in the narrow structure gaps, accelerating droplet spreading. Third, the confinement effect forces the liquid to spread over the dry region inaccessible on a smooth surface, increasing the uniformity and preventing dryout. This works on both micro- and macrostructured surfaces. However, on microstructured surfaces, the liquid film thickness is more comparable to the structure sizes, where this phenomenon may present a more obvious effect. For instance, Chen et al. [87] found that both the spreading speed and wetting area of droplets on hybrid micro/nanostructured surfaces are higher than those on nanowire arrayed surfaces as a result of the "channeling effect." Accordingly, the hybrid surfaces showed a higher CHF than the nanowire arrayed surfaces.

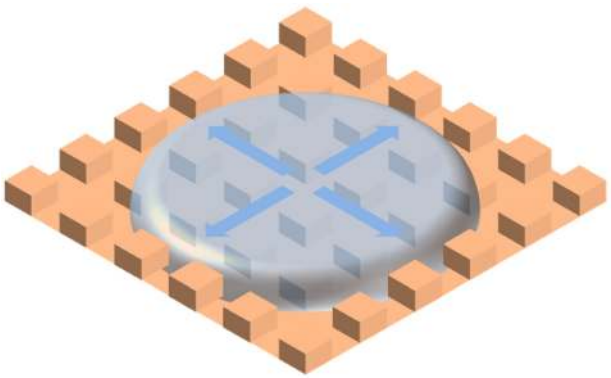

Fig. 26 Schematic of the flow confinement effect of microstructured surfaces

4.6 Wickability Enhancement. Another critical influence of surface structures is the capillary pressure induced by the meniscus built-up in the gaps within the structured layer. The capillary pressure ΔP_{cap} is proportional to σ/r_{cur}, where σ is the surface tension and r_{cur} is the radius of curvature of the meniscus, which is in the same order as the gap width. Therefore, the narrower the structure gaps are, the stronger the capillary pressure is, which can induce a stronger capillary force that accelerates the spreading of liquid in the structured layer. This force becomes dominant when the capillary pressure in the structured layer dominates over the capillary pressure in the upper droplet. For instance, their ratio reaches the order of 1 and 100 for structure gaps of tens of micrometers and hundreds of nanometers, respectively, for a typical spray droplet diameter of 50 μm. Thus, the capillary force exerts a mild influence on microstructured surfaces and becomes dominant on nanostructured surfaces.

Another way to evaluated the relative dominance of the capillary effect is by energy analysis, which can be achieved by comparing the surface energy of the structured layer with the upper droplet gravitational potential energy (altered Bond number Bo*), kinetic energy (altered Weber number We*), and surface energy of the droplet (Z^*) [147]

$$\mathrm{Bo}^* = \frac{\rho_l g r_d^2}{b\Delta P_{cap}},\ \mathrm{We}^* = \frac{r_d \rho_l u_d^2}{b\Delta P_{cap}},\ Z^* = \frac{\sigma}{b\Delta P_{cap}} \tag{4}$$

where ρ_l is the density of the droplet, g is the gravitational acceleration, r_d is the initial droplet radius, b is the thickness of the structured layer, ΔP_{cap} is the capillary pressure, u_d is the initial droplet velocity and σ is the surface tension. For a nanostructured surface, capillarity is a dominant factor [147], and these dimensionless numbers are all much less than 1, meaning that the gravitational, kinetic and bulk surface energies can be neglected compared to the surface energy of the structured layer. The strong capillary pressure in the structured layer provides the driving force for liquid advancement against viscous resistance, creating a so-called hemispreading or capillary wicking region beyond the upper droplet contact line [87,129,138,147–149], as shown in Fig. 14(*f*). This driving force can increase the spreading velocity of the upper droplet region, which is characterized as the wickability of the surface [147], which can describe the wettability of superhydrophilic nanostructured surfaces whose contact angles are very close to zero [87].

The wickability ω^* is theoretically related to system parameters as shown in the following equation:

$$\omega^* = \frac{\sqrt{2}\kappa\Delta P_{cap}}{b\varepsilon\mu_l} \tag{5}$$

where κ is the permeability of the structured layer, ε is the porosity of the structured layer and μ_l is the dynamic viscosity of the liquid. Compared with microstructures, a nanostructured layer has a higher ΔP_{cap} and a lower b, which leads to a better wickability of 200–300 mm/s [129,149]. As shown in Fig. 27, the enhancement of the wickability on nanostructures enables rapid wetting

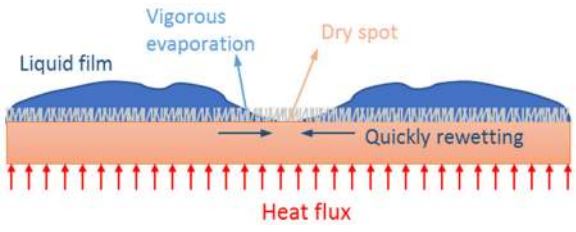

Fig. 27 Schematic of the enhancement mechanisms of nanostructured surfaces (Reproduced with permission from Ref. [87]. Copyright 2006 by Elsevier.)

and rewetting of dry spots on hot surfaces, helping to create a uniform temperature distribution and prevent the dryout-induced CHF. The hemispreading region not only enlarges the wetted area but also enables high heat flux in these areas since the thin liquid film in the structured layer evaporates significantly due to the ultralow heat and mass transfer resistance. Chen et al. [138] found that the evaporation rate of a microscale droplet could be greatly enhanced with the presence of precursor film on a nanoporous surface. In summary, the superior wickability is the unique merit of nanostructured surfaces in spray cooling, whereas capillarity has limited effects on microstructured surfaces.

4.7 Summary of Enhancement Mechanisms. The mechanisms summarized above as well as the length scales of physical processes in spray cooling are presented in Fig. 28 to give a clear map of spray cooling enhancement mechanisms for engineered surfaces with different characteristic structure sizes. In summary, the dominant spray cooling enhancement mechanisms are improved wickability for nanostructured surfaces; increased triple contact line length, active nucleation sites, and flow confinement for microstructured surfaces; and enlarged surface area, flow confinement, and triple contact line length for macrostructured surfaces. Fortunately, these merits can be integrated into one hierarchical structured surface, as reviewed in Sec. 2.3. However, the investigations of hierarchical structures are far from adequate, leaving much room for further research and development. It should be noted that given these enhancement mechanisms, one could not only design advanced surface structures to enhance spray cooling performance but also select proper spray characteristics that are suitable for specific surfaces to strengthen specific heat transfer mechanisms.

5 Conclusion and Future Concerns

With the increasing demands for ultrahigh heat flux cooling, surface engineering-enhanced spray cooling has become a promising cooling technique for next-generation high-power devices. In this paper, the progress in and mechanisms of spray cooling enhancement via surface engineering are reviewed, analyzed, and clarified.

The physical characteristic lengths in the spray cooling process range from the nanometer scale to the millimeter scale and the dominant forces and transport mechanisms may vary on surfaces with different structure length scales. The influences of engineered surfaces are reviewed for millimeter-, micrometer- and nanometer-scale structured surfaces and hierarchical structured surfaces with respect to different manufacturing methods. Various engineered surfaces can enhance the spray cooling CHF, HTC, and cooling efficiency. Based on the collected data, the CHF and HTC of spray cooling are of the order of 100-1000 W/cm^2 and 1–100 W/cm^2K, respectively, which can meet the current electronic cooling demands and are very promising for meeting next-generation power electronic cooling demands with further development. The cooling efficiency decreases with increasing coolant mass flux or CHF. Fortunately, the frontier of the CHF-η plot can be extended by introducing surface structures. The effects of spray type and working fluid are also analyzed. The reviewed data show that spray cooling can achieve a CHF above 945.7 W/cm^2 and an HTC up to 57 W/cm^2K on structured surfaces without the assistance of secondary gas flow and a CHF and an HTC up to 1250.1 W/cm^2 and 250W/cm^2K, respectively, on a smooth surface with the assistance of secondary gas flow. A CHF enhancement up to 110% was achieved on a hybrid micro- and nanostructured surface.

Multiple enhancement mechanisms are discussed and clarified based on analysis and comparison of dimensions between characteristic physical lengths in the spray cooling process and structure sizes. Low contact angles are preferred in pressure-atomized spray cases, while for gas-atomized spray, they may cause a decrease in nucleate boiling heat transfer. The dominant spray cooling enhancement mechanisms are improved wickability for nanostructured surfaces; increased triple contact line length, active nucleation sites, and flow confinement for microstructured surfaces; and enlarged surface area, flow confinement and triple contact line length for macrostructured surfaces. A clear map of mechanisms related to the scales of surface structures is provided in Fig. 28.

This work reviews the progress in surface engineering-enhanced spray cooling, which has been validated to be efficient in multiple cooling applications, especially at high heat fluxes with limited coolant flow rates. With detailed discussions, the progress in and mechanisms of spray cooling on engineered surfaces are presented with a clear structure, which helps the understanding and design of engineered surfaces and selection of proper spray characteristics for a given surface in spray cooling and provides insights for interdisciplinary applications of heat transfer and advanced engineering materials. It should be noted that this

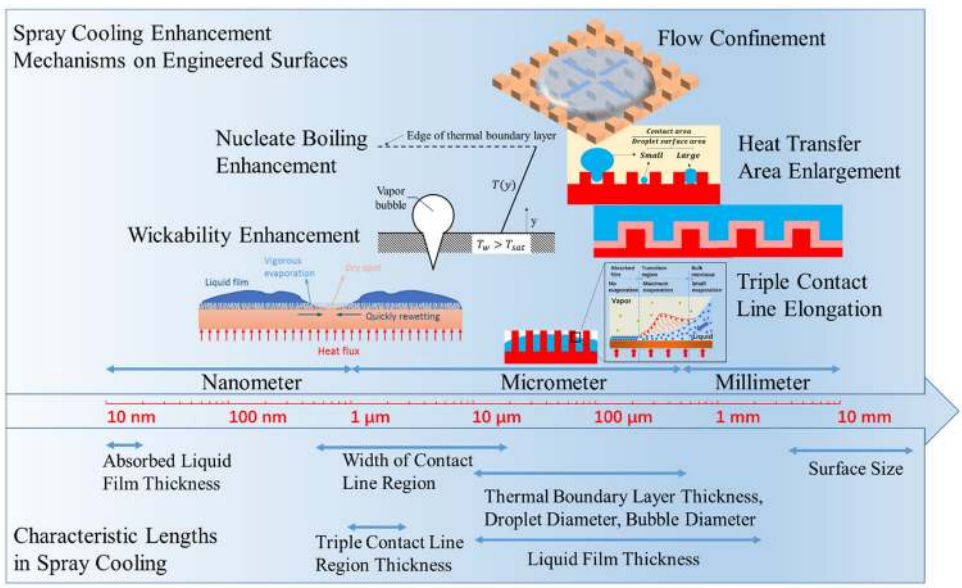

Fig. 28 Spray cooling enhancement mechanism map of engineered surfaces with different characteristic structure sizes and related physical length scales

review focus on experimental efforts and theoretical efforts on the fluid mechanics of spray cooling or droplet impact process is not the main focus of the review. However, spray cooling phenomena are analyzed from fluid mechanics and heat transfer point-of-view to illustrate the diverse spray cooling mechanisms.

For the further development of high heat flux spray cooling and application of this technique in advanced industrial and defense-related domains such as high-performance chip, radar, and laser unit, spray cooling needs to be further investigated and improved in multiple aspects. First, surface engineering investigations should be continued with an emphasis on hierarchical structures that can combine enhancement mechanisms at different length scales while considering scalability, durability, and smart and rapid responses to transient environmental conditions. Next, for the integration of spray cooling modules with high-power devices, spray cooling systems need to be simplified and downsized, and the system loop and spray generation parts need to be recreated to meet this goal. Last, with the transient and severe thermal loads applied on the spray cooling module, a self-adaption capability, as well as, smart and rapid control strategies are of vital importance for a spray system to be capable and efficient, which requires further development. Fortunately, the abovementioned aspects have drawn increasing attention. Scalable heat transfer-enhancing surfaces with high performance have been invented for pool boiling [150], condensation heat transfer [151], and solar steam generation [152], which inspire the design of spray cooling surfaces with similar merits. Piezo-electric spraying [17,71,153] and electrospraying [73,74] are proposed as two promising ways to achieve efficient and small-sized spray cooling. Jiang et al. [20] designed a novel spray cooling plate that can be integrated on active phased array radar, and the radar was controlled below 43 °C while a heat flux of 323.3 W/cm^2 was dissipated. Huddle et al. [10] designed and simulated pressure-atomized ammonia spray cooling of a laser array that generates a heat flux over 1700 W/cm^2 on each laser emitter, proving the feasibility of cooling high power laser array using a spray chamber. Besides, recent advances in single phase microchannel cooling integrated with electronic design [154] have also shed light on the codesigning of electronics with phase-change cooling, which is a promising pathway for electronic cooling using spray cooling. Intermittent spray cooling has been studied as a straightforward spray control and coolant-saving strategy [61,62,155]. Recently, Tsang and Sun [156] proposed and studied intermittent spray cooling using a self-rewetting inverse-Marangoni fluid and found that with a self-rewetting fluid, a larger surface area could be cooled without an increase in the number of nozzles, and surface temperatures were controlled to be lower, more uniform and more stable. Despite the progress in intermittent spray cooling, the control of the spray system according to external environment variations needs to be further developed, either by applying an advanced algorithm to realize initiative control or by designing the system based on the physical nature to realize self-adaptive cooling, which can be inspired by capillary-induced self-pumping transpiration cooling [157].

Funding Data

- National Natural Science Foundation of China for Excellent Young Scientist (Grant No. 51722602; Funder ID: 10.13039/501100001809).

Nomenclature

A_{TBL} = the area of the thermal boundary layer (mm^2)
b = thickness of the structured layer (μm)
Bo* = altered Bond number, Bo*= $\frac{\rho_l g r_d^2}{b\Delta P_{cap}}$
g = gravitational acceleration (m/s^2)
h = heat transfer coefficient (W/cm^{2}K)
h_{fg} = latent heat of vaporization (kJ/kg)
$h_l(T_{in})$ = inlet coolant liquid enthalpy
$h_v(T_w)$ = enthalpy of the coolant vapor when it is heated to the wall temperature
$\dot{m}''$ = coolant mass flux (kg/m^{2}s)
P_l = liquid pressure (Pa)
q = heat flux (W/cm^2)
Q = heat flow (W)
$r_{c,max}$ = upper bound of the active cavity size (μm)
$r_{c,min}$ = lower bound of the active cavity size (μm)
r_{cur} = radius of curvature of the meniscus (μm)
r_d = initial droplet radius (mm)
T_{in} = inlet temperature (K)
$T_{sat}(P_l)$ = saturation temperature of the liquid at a pressure of P_l (K)
T_w = wall temperature (K)
T_∞ = ambient temperature (K)
u_d = initial droplet velocity (m/s)
We* = altered Weber number, We* = $\frac{r_d \rho_l u_d^2}{b\Delta P_{cap}}$
Z* = dimensionless number representing ratios of surface energy of the structured layer over surface energy of the droplet, $Z^* = \frac{\sigma}{b\Delta P_{cap}}$
ΔP_{cap} = capillary pressure (Pa)

Greek Symbols

δ_T = thermal boundary layer thickness (μm)
ε = porosity of the structured layer (%)
η = cooling efficiency (%)
κ = permeability of the structured layer (D)
λ_l = thermal conductivity of the liquid (W/mK)
μ_l = dynamic viscosity of the liquid (Pa·s)
ρ_l = liquid density (kg/m^3)
ρ_v = vapor density (kg/m^3)
σ = surface tension (N/m) $\theta_{sat} = \theta_{sat} = T_{sat}(P_l) - T_\infty$
$\theta_w = \theta_w = T_w - T_\infty$
ω^* = wickability, $\omega^* = \frac{\sqrt{2}\kappa\Delta P_{cap}}{b\varepsilon\mu_l}$

Abbreviations

CA = contact angle (deg)
CHF = critical Heat flux (W/cm^2)
DRIE = deep reactive ion etching
EDM = electrical discharge machining
GNPs = graphene nanoplatelets
HTC = heat transfer coefficient (W/cm^{2}K)
MEMS = microelectromechanical systems
PAN = polyacrylonitrile

References

[1] Liang, G. T., and Mudawar, I., 2017, "Review of Spray Cooling—Part 1: Single-Phase and Nucleate Boiling Regimes, and Critical Heat Flux," Int. J. Heat Mass Transfer, **115**, pp. 1174–1205.
[2] Sehmbey, M. S., Chow, L. C., Pais, M. R., and Mahefkey, T., 1995, "High Heat Flux Spray Cooling of Electronics," AIP Conf. Proc., **324**(1), pp. 903–909.
[3] Toda, S., 1972, "A Study of Mist Cooling: 1st Report, Experimental Investigations on Mist Cooling by Mist Flow Sprayed Vertically on Small and Flat Plates Heated at High Temperatures," Trans. Jpn. Soc. Mech. Eng., **38**(307), pp. 581–588.
[4] Zhirnov, V. V., Cavin, R. K., Hutchby, J. A., and Bourianoff, G. I., 2003, "Limits to Binary Logic Switch Scaling—A Gedanken Model," Proc. IEEE, **9**(11), pp. 1934–1939.
[5] Silk, E. A., Golliher, E. L., and Selvam, R. P., 2008, "Spray Cooling Heat Transfer: Technology Overview and Assessment of Future Challenges for Micro-Gravity Application," Energy Convers. Manage, **49**(3), pp. 453–468.
[6] Wang, J. X., Li, Y. Z., Mao, Y. F., Li, E. H., Ning, X. W., and Ji, X. Y., 2018, "Comparative Study of the Heating Surface Impact on Porous-Material-Involved Spray System for Electronic Cooling—An Experimental Approach," Appl. Therm. Eng., **135**, pp. 537–548.
[7] Hsieh, S. S., and Luo, S. Y., 2016, "Droplet Impact Dynamics and Transient Heat Transfer of a Micro Spray System for Power Electronics Devices," Int. J. Heat Mass Transfer, **92**, pp. 190–205.
[8] Bloschock, K., and Bar-Cohen, A., 2012, "Advanced Thermal Management Technologies for Defense Electronics," SPIE Paper No. 84050I.

[9] Huddle, J. J., Chow, L. C., Lei, S., Marcos, A., Rini, D. P., Lindauer, S. J., Bass, M., and Delfyett, P. J., 2000, "Thermal Management of Diode Laser Arrays," Sixteenth Annual IEEE Semiconductor Thermal Measurement and Management Symposium (Cat. No.00CH37068), San Jose, CA, Mar. 23, pp. 154–160.
[10] Bar-Cohen, A., Maurer, J. J., and Felbinger, J. G., 2013, "DARPA's Intra/Interchip Enhanced Cooling (ICECOOL) Program," International Conference on Compound Semiconductor Manufacturing Technology, (CS MANTECH 2013), New Orlens, LA, May 13–16, pp. 171–174.
[11] Kim, J. H., 2007, "Spray Cooling Heat Transfer: The State of the Art," Int. J. Heat Fluid Flow, **28**(4), pp. 753–767.
[12] Mudawar, I., 2013, "Recent Advances in High-Flux, Two-Phase Thermal Management," ASME J. Therm. Sci. Eng. Appl., **5**(2), p. 021012.
[13] Cheng, W. L., Zhang, W. W., Chen, H., and Hu, L., 2016, "Spray Cooling and Flash Evaporation Cooling: The Current Development and Application," Renewable Sustainable Energy Rev., **55**, pp. 614–628.
[14] Cader, T., Westra, L. J., and Eden, R. C., 2004, "Spray Cooling Thermal Management for Increased Device Reliability," IEEE Trans. Device Mater. Reliab., **4**(4), pp. 605–613.
[15] Chen, S. J., and Tseng, A. A., 1992, "Spray and Jet Cooling in Steel Rolling," Int. J. Heat Fluid Flow, **13**(4), pp. 358–369.
[16] Lay, K. K., Cheong, B. M. Y., Tong, W. L., Tan, M. K., and Hung, Y. M., 2017, "Effective Micro-Spray Cooling for Light-Emitting Diode With Graphene Nanoporous Layers," Nanotechnology, **28**(16), p. 164003.
[17] Chen, J. N., 2017, "Experimental Investigation and Mechanism Study of Spray Cooling With Mircro-Nano Structured and Chemical Modified Surfaces," Ph.D. thesis, Tsinghua University, Beijing, China.
[18] Mudawar, I., Bharathan, D., Kelly, K., and Narumanchi, S., 2009, "Two-Phase Spray Cooling of Hybrid Vehicle Electronics," IEEE Trans. Compon. Packaging Technol., **32**(2), pp. 501–512.
[19] Jiang, S. L., Li, J., Xiao, R., Leng, T. T., Zhong, J. F., and Cheng, W. L., 2019, "Novel Spray Cooling Plate for Thermal Control of Active Phased Array Radar," IOP Conf. Ser. Mater. Sci. Eng., **677**, p. 022093.
[20] Lei, S., Shi, Y., and Chen, G., 2020, "A Lithium-Ion Battery-Thermal-Management Design Based on Phase-Change-Material Thermal Storage and Spray Cooling," Appl. Therm. Eng., **168**, p. 114792.
[21] Yang, X., and Yan, Y. Y., 2011, "Molecular Dynamics Simulation for Microscope Insight of Water Evaporation on a Heated Magnesium Surface," Appl. Therm. Eng., **31**(5), pp. 640–648.
[22] Pautsch, A. G., and Shedd, T. A., 2006, "Adiabatic and Diabatic Measurements of the Liquid Film Thickness During Spray Cooling With FC-72," Int. J. Heat Mass Transfer, **49**(15–16), pp. 2610–2618.
[23] Hsieh, S. S., Chen, G. W., and Yeh, Y. F., 2015, "Optical Flow and Thermal Measurements for Spray Cooling," Int. J. Heat Mass Transfer, **87**, pp. 248–253.
[24] Yang, J., Chow, L. C., Pais, M. R., and Ito, A., 1992, "Liquid Film Thickness and Topography Determination Using Fresnel Diffraction and Holography," Exp. Heat Transfer, **5**(4), pp. 239–252.
[25] Martínez-Galván, E., Ramos, J. C., Antón, R., and Khodabandeh, R., 2013, "Influence of Surface Roughness on a Spray Cooling System With R134a. Part II: Film Thickness Measurements," Exp. Therm. Fluid Sci., **48**, pp. 73–80.
[26] Hou, Y., Tao, Y. J., and Huai, X. L., 2013, "Visualization of Film Wavelike Characteristics and Measurement of Film Thickness in Spray Cooling," J. Therm. Sci., **22**(2), pp. 186–195.
[27] Pais, M. R., Chow, L. C., and Mahefkey, E. T., 1992, "Surface-Roughness and Its Effects on the Heat-Transfer Mechanism in Spray Cooling," ASME J. Heat Transfer, **114**(1), pp. 211–219.
[28] Rini, D. P., Chen, R. H., and Chow, L. C., 2002, "Bubble Behavior and Nucleate Boiling Heat Transfer in Saturated FC-72 Spray Cooling," ASME J. Heat Transfer, **124**(1), pp. 63–72.
[29] Yang, J., Chow, L. C., and Pais, M. R., 1996, "Nucleate Boiling Heat Transfer in Spray Cooling," ASME J. Heat Transfer, **118**(3), pp. 668–671.
[30] Pautsch, A. G., and Shedd, T. A., 2005, "Spray Impingement Cooling With Single- and Multiple-Nozzle Arrays. Part I: Heat Transfer Data Using FC-72," Int. J. Heat Mass Transfer, **48**(15), pp. 3167–3175.
[31] Selvam, R. P., Lin, L. C., and Ponnappan, R., 2005, "Computational Modeling of Spray Cooling: Current Status and Future Challenges," *Space Technology and Applications International Forum-Staif 2005*, M. S. ElGenk, ed., Amer Inst Physics, Melville, pp. 55–63.
[32] Selvam, R. P., Lin, L. C., and Ponnappan, R., 2006, "Direct Simulation of Spray Cooling: Effect of Vapor Bubble Growth and Liquid Droplet Impact on Heat Transfer," Int. J. Heat Mass Transfer, **49**(23–24), pp. 4265–4278.
[33] Xie, N. N., Hu, X. G., and Tang, D. W., 2011, "Visualization of Microbubble Dynamics Behavior in Rectangular Capillary Microgrooves Under Spray Cooling Condition," Heat Transfer Eng., **32**(11–12), pp. 1019–1025.
[34] Pais, M., Tilton, D., Chow, L., and Mahefkey, E., 1989, "High-Heat-Flux, Low-Superheat Evaporative Spray Cooling," AIAA Paper No. AIAA-89-0241.
[35] Tilton, D. E., 1989, "*Spray Cooling*," Ph.D. thesis, University of Kentucky, Lexington, KY.
[36] Estes, K. A., and Mudawar, I., 1995, "Comparison of Two-Phase Electronic Cooling Using Free Jets and Sprays," ASME J. Electron Packag., **117**(4), pp. 323–332.
[37] Putnam, S. A., Briones, A. M., Byrd, L. W., Ervin, J. S., Hanchak, M. S., White, A., and Jones, J. G., 2012, "Microdroplet Evaporation on Superheated Surfaces," Int. J. Heat Mass Transfer, **55**(21–22), pp. 5793–5807.
[38] Lin, L. C., and Ponnappan, R., 2003, "Heat Transfer Characteristics of Spray Cooling in a Closed Loop," Int. J. Heat Mass Transfer, **46**(20), pp. 3737–3746.
[39] Visaria, M., and Mudawar, I., 2009, "Application of Two-Phase Spray Cooling for Thermal Management of Electronic Devices," IEEE Trans. Compon. Packaging Technol., **32**(4), pp. 784–793.
[40] Wu, W., Bostanci, H., Chow, L. C., Ding, S. J., Hong, Y., Su, M., Kizito, J. P., Gschwender, L., and Snyder, C. E., 2011, "Jet Impingement and Spray Cooling Using Slurry of Nanoencapsulated Phase Change Materials," Int. J. Heat Mass Transfer, **54**(13–14), pp. 2715–2723.
[41] Cheng, W. L., Xie, B., Han, F. Y., and Chen, H., 2013, "An Experimental Investigation of Heat Transfer Enhancement by Addition of High-Alcohol Surfactant (HAS) and Dissolving Salt Additive (DSA) in Spray Cooling," Exp. Therm. Fluid Sci., **45**, pp. 198–202.
[42] Ravikumar, S. V., Haldar, K., Jha, J. M., Chakraborty, S., Sarkar, I., Pal, S. K., and Chakraborty, S., 2015, "Heat Transfer Enhancement Using Air-Atomized Spray Cooling With Water-Al_2O_3 Nanofluid," Int. J. Therm. Sci., **96**, pp. 85–93.
[43] Hsieh, S. S., Leu, H. Y., and Liu, H. H., 2015, "Spray Cooling Characteristics of Nanofluids for Electronic Power Devices," Nanoscale Res. Lett., **10**, pp. 1–16.
[44] Sadafi, M. H., Ruiz, S. G., Vetrano, M. R., Jahn, I., van Beeck, J., Buchlin, J. M., and Hooman, K., 2016, "An Investigation on Spray Cooling Using Saline Water With Experimental Verification," Energy Convers. Manag., **108**, pp. 336–347.
[45] Tseng, A. A., Bellerova, H., Pohanka, M., and Raudensky, M., 2014, "Effects of Titania Nanoparticles on Heat Transfer Performance of Spray Cooling With Full Cone Nozzle," Appl. Therm. Eng., **62**(1), pp. 20–27.
[46] Bhatt, N. H., Lily, Raj, R., Varshney, P., Pati, A. R., Chouhan, D., Kumar, A., Munshi, B., and Mohapatra, S. S., 2017, "Enhancement of Heat Transfer Rate of High Mass Flux Spray Cooling by Ethanol-Water and Ethanol-Tween20-Water Solution at Very High Initial Surface Temperature," Int. J. Heat Mass Transfer, **110**, pp. 330–347.
[47] Duursma, G., Sefiane, K., and Kennedy, A., 2009, "Experimental Studies of Nanofluid Droplets in Spray Cooling," Heat Transf. Eng., **30**(13), pp. 1108–1120.
[48] Tian, J. M., Chen, B., Li, D., and Zhou, Z. F., 2017, "Transient Spray Cooling: Similarity of Dynamic Heat Flux for Different Cryogens, Nozzles and Substrates," Int. J. Heat Mass Transfer, **108**, pp. 561–571.
[49] Ashwood, A. C., and Shedd, T. A., 2007, "Spray Cooling With Mixtures of Dielectric Fluids," Proceedings of 23 Annual IEEE Semiconductor Thermal Measurement and Management Symposium, San Jose, CA, Mar. 18–22, p. 144.
[50] Tsang, S., Wu, Z. H., Lin, C. H., and Sun, C. L., 2018, "On the Evaporative Spray Cooling With a Self-Rewetting Fluid: Chasing the Heat," Appl. Therm. Eng., **132**, pp. 196–208.
[51] Bostanci, H., He, B., and Chow, L. C., 2017, "Spray Cooling With Ammonium Hydroxide," Int. J. Heat Mass Transfer, **107**, pp. 45–52.
[52] Panao, M. R. O., Costa, J. J., and Bernardo, M. R. F., 2018, "Thermal Assessment of Sublimation Cooling With Dry-Ice Sprays," Int. J. Heat Mass Transfer, **118**, pp. 518–526.
[53] Zhang, W. W., Li, Y. Y., Long, W. J., and Cheng, W. L., 2018, "Enhancement Mechanism of High Alcohol Surfactant on Spray Cooling: Experimental Study," Int. J. Heat Mass Transfer, **126**, pp. 363–376.
[54] Liu, H., Cai, C., Jia, M., Gao, J. L., Yin, H. C., and Chen, H., 2019, "Experimental Investigation on Spray Cooling With Low-Alcohol Additives," Appl. Therm. Eng., **146**, pp. 921–930.
[55] Peng, Y. H., and Cheng, W. L., 2017, "Experimental Investigation on the Effect of Heat Transfer Enhancement of Vacuum Spray Flash Evaporation Cooling Using Al_2O_3-Water Nanofluid," J. Energy Procedia, **142**, pp. 3766–3773.
[56] Wang, C., Song, Y., and Jiang, P. X., 2018, "Modelling of Liquid Nitrogen Spray Cooling in an Electronic Equipment Cabin Under Low Pressure," Appl. Therm. Eng., **136**, pp. 319–326.
[57] Estes, K. A., and Mudawar, I., 1995, "Correlation of Sauter Mean Diameter and Critical Heat-Flux for Spray Cooling of Small Surfaces," Int. J. Heat Mass Transfer, **38**(16), pp. 2985–2996.
[58] Chen, R. H., Chow, L. C., and Navedo, J. E., 2002, "Effects of Spray Characteristics on Critical Heat Flux in Subcooled Water Spray Cooling," Int. J. Heat Mass Transfer, **45**(19), pp. 4033–4043.
[59] Ghodbane, M., and Holman, J. P., 1991, "Experimental-Study of Spray Cooling With Freon-113," Int. J. Heat Mass Transfer, **34**(4–5), pp. 1163–1174.
[60] Zhang, Z., Jiang, P. X., Hu, Y. T., and Li, J., 2013, "Experimental Investigation of Continual- and Intermittent-Spray Cooling," Exp. Heat Transfer, **26**(5), pp. 453–469.
[61] Panao, M. R. O., and Moreira, A. L. N., 2009, "Intermittent Spray Cooling: A New Technology for Controlling Surface Temperature," Int. J. Heat Fluid Flow, **30**(1), pp. 117–130.
[62] Shedd, T. A., and Pautsch, A. G., 2005, "Spray Impingement Cooling With Single- and Multiple-Nozzle Arrays. Part II: Visualization and Empirical Models," Int. J. Heat Mass Transfer, **48**(15), pp. 3176–3184.
[63] Amon, C. H., Yao, S. C., Wu, C. F., and Hsieh, C. C., 2005, "Microelectromechanical System-Based Evaporative Thermal Management of High Heat Flux Electronics," ASME J. Heat Transfer, **127**(1), pp. 66–75.
[64] Tsukamoto, K., Kita, Y., Inoue, S., Hamanosono, T., Hidaka, S., Ueoka, S., Fukuda, H., Kohno, M., and Takata, Y., 2020, "On the Onset of Quench During Spray Cooling: The Significance of Oxide Layers," Appl. Therm. Eng., **179**, p. 115682.

[65] Mertens, R. G., Chow, L., Sundaram, K. B., Cregger, R. B., Rini, D. P., Turek, L., and Saarloos, B. A., 2007, "Spray Cooling of IGBT Devices," ASME J. Electron Packag., **129**(3), pp. 316–323.
[66] Wang, J. X., Li, Y. Z., Zhang, H. S., Wang, S. N., Mao, Y. F., Zhang, Y. N., and Liang, Y. H., 2015, "Investigation of a Spray Cooling System With Two Nozzles for Space Application," Appl. Therm. Eng., **89**, pp. 115–124.
[67] Bostanci, H., Van Ee, D., Saarloos, B. A., Rini, D. P., and Chow, L. C., 2012, "Thermal Management of Power Inverter Modules at High Fluxes Via Two-Phase Spray Cooling," IEEE Trans. Compon. Packag. Manuf., **2**(9), pp. 1480–1485.
[68] Turek, L. J., Rini, D. P., Saarloos, B. A., and Chow, L. C., 2008, "Evaporative Spray Cooling of Power Electronics Using High Temperature Coolant," 11th IEEE Intersociety Conference on Thermal and Thermomechanical Phenomena in Electronic Systems, Vols. 1–3, Orlando, FL, May 28–31, p. 346.
[69] Wang, J. X., Li, Y. Z., Li, G. C., Xiong, K., and Ning, X. W., 2017, "Investigation of a Gravity-Immune Chip-Level Spray Cooling for Thermal Protection of Laser-Based Wireless Power Transmission System," Int. J. Heat Mass Transfer, **114**, pp. 715–726.
[70] Chen, H., Cheng, W. L., Peng, Y. H., Zhang, W. W., and Jiang, L. J., 2016, "Experimental Study on Optimal Spray Parameters of Piezoelectric Atomizer Based Spray Cooling," Int. J. Heat Mass Transfer, **103**, pp. 57–65.
[71] Wang, J. X., Li, Y. Z., Li, J. X., Li, C., Xiong, K., and Ning, X. W., 2018, "Enhanced Heat Transfer by an Original Immersed Spray Cooling System Integrated With an Ejector," Energy, **158**, pp. 512–523.
[72] Wang, H. C., and Mamishev, A. V., 2012, "Heat Transfer Correlation Models for Electrospray Evaporative Cooling Chambers of Different Geometry Types," Appl. Therm. Eng., **40**, pp. 91–101.
[73] Deng, W. W., and Gomez, A., 2011, "Electrospray Cooling for Microelectronics," Int. J. Heat Mass Transfer, **54**(11–12), pp. 2270–2275.
[74] Wang, C., Xu, R. N., Song, Y., and Jiang, P. X., 2017, "Study on Water Droplet Flash Evaporation in Vacuum Spray Cooling," Int. J. Heat Mass Transfer, **112**, pp. 279–288.
[75] Ang, K. M., Yeo, L. Y., Friend, J. R., Hung, Y. M., and Tan, M. K., 2015, "Nozzleless Spray Cooling Using Surface Acoustic Waves," J. Aerosol Sci., **79**, pp. 48–60.
[76] Breitenbach, J., Roisman, I. V., and Tropea, C., 2017, "Heat Transfer in the Film Boiling Regime: Single Drop Impact and Spray Cooling," Int. J. Heat Mass Transfer, **110**, pp. 34–42.
[77] Breitenbach, J., Roisman, I. V., and Tropea, C., 2017, "Drop Collision With a Hot, Dry Solid Substrate: Heat Transfer During Nucleate Boiling," Phys. Rev. Fluids, **2**(7), p. 074301.
[78] Breitenbach, J., Roisman, I. V., and Tropea, C., 2018, "From Drop Impact Physics to Spray Cooling Models: A Critical Review," Exp. Fluids, **59**(3), p. 21.
[79] Karchevsky, A. L., Marchuk, I. V., and Kabov, O. A., 2016, "Calculation of the Heat Flux Near the Liquid-Gas-Solid Contact Line," Appl. Math. Model., **40**(2), pp. 1029–1037.
[80] Tien, C. L., 1962, "A Hydrodynamic Model for Nucleate Pool Boiling," Int. J. Heat Mass Transfer, **5**(6), pp. 533–540.
[81] Jo, H., Kaviany, M., Kim, S. H., and Kim, M. H., 2014, "Heterogeneous Bubble Nucleation on Ideally-Smooth Horizontal Heated Surface," Int. J. Heat Mass Transfer, **71**, pp. 149–157.
[82] Selvam, R. P., Sarkar, M., Sarkar, S., Ponnappan, R., and Yerkes, K. L., 2009, "Modeling Thermal-Boundary-Layer Effect on Liquid-Vapor Interface Dynamics in Spray Cooling," J. Thermophys. Heat Transfer, **23**(2), pp. 356–370.
[83] Zhang, Z., Li, J., and Jiang, P. X., 2013, "Experimental Investigation of Spray Cooling on Flat and Enhanced Surfaces," Appl. Therm. Eng., **51**(1–2), pp. 102–111.
[84] Jia, W., and Qiu, H. H., 2003, "Experimental Investigation of Droplet Dynamics and Heat Transfer in Spray Cooling," Exp. Therm. Fluid Sci., **27**(7), pp. 829–838.
[85] Carey, V. P., 2020, *Liquid-Vapor Phase-Change Phenomena: An Introduction to the Thermophysics of Vaporization and Condensation Processes in Heat Transfer Equipment*, CRC Press, Boca Raton, FL.
[86] Chen, J. N., Xu, R. N., Zhang, Z., Chen, X., Ouyang, X. L., Wang, G. Y., and Jiang, P. X., 2018, "Phenomenon and Mechanism of Spray Cooling on Nanowire Arrayed and Hybrid Micro/Nanostructured Surfaces," ASME J. Heat Transfer, **140**(11), p. 112401.
[87] Silk, E. A., Kim, J., and Kiger, K., 2006, "Spray Cooling of Enhanced Surfaces: Impact of Structured Surface Geometry and Spray Axis Inclination," Int. J. Heat Mass Transfer, **49**(25–26), pp. 4910–4920.
[88] Silk, E. A., Kim, J., and Kiger, K., 2006, "Enhanced Surface Spray Cooling With Embedded and Compound Extended Surface Structures," Thermal and Thermomechanical Proceedings 10th Intersociety Conference on Phenomena in Electronics Systems, ITHERM, San Diego, CA, May 30–June 2, pp. 215–223.
[89] Silk, E. A., 2008, "Investigation of Pore Size Effect on Spray Cooling Heat Transfer With Porous Tunnels," Space Technology and Applications International Forum Staif, M. S. ElGenk, ed., American Institute of Physics, Melville, pp. 112–122.
[90] Wang, Y., Zhou, N. Y., Yang, Z., and Jiang, Y. L., 2016, "Experimental Investigation of Aircraft Spray Cooling System With Different Heating Surfaces and Different Additives," Appl. Therm. Eng., **103**, pp. 510–521.
[91] Aamir, M., Liao, Q., Hong, W., Xun, Z., Song, S. H., and Sajid, M., 2017, "Transient Heat Transfer Behavior of Water Spray Evaporative Cooling on a Stainless Steel Cylinder With Structured Surface for Safety Design Application in High Temperature Scenario," Heat Mass Transfer, **53**(2), pp. 363–375.
[92] Aamir, M., Qiang, L., Hong, W., Xun, Z., Wang, J. Q., and Sajid, M., 2017, "Transient Heat Transfer Performance of Stainless Steel Structured Surfaces Combined With Air-Water Spray Evaporative Cooling at High Temperature Scenarios," Appl. Therm. Eng., **115**, pp. 418–434.
[93] Xie, J. L., Tan, Y. B., Duan, F., Ranjith, K., Wong, T. N., Toh, K. C., Choo, K. F., and Chan, P. K., 2013, "Study of Heat Transfer Enhancement for Structured Surfaces in Spray Cooling," Appl. Therm. Eng., **59**(1–2), pp. 464–472.
[94] Zhang, Y., Pang, L. P., Liu, M., and Xie, Y. Q., 2016, "Investigation of Spray Cooling: Effect of Different Heater Surfaces Under Acceleration," Int. Commun. Heat Mass Transfer, **75**, pp. 223–231.
[95] Ortiz, L., and Gonzalez, J. E., 1999, "Experiments on Steady-State High Heat Fluxes Using Spray Cooling," Exp. Heat Transfer, **12**(3), pp. 215–233.
[96] Martinez-Galvan, E., Anton, R., Ramos, J. C., and Khodabandeh, R., 2013, "Influence of Surface Roughness on a Spray Cooling System With R134a. Part I: Heat Transfer Measurements," Exp. Therm. Fluid Sci., **46**, pp. 183–190.
[97] Sehmbey, M. S., Chow, L. C., Hahn, O. J., and Pais, M. R., 1995, "Effect of Spray Characteristics on Spray Cooling With Liquid-Nitrogen," J. Thermophys. Heat Transfer, **9**(4), pp. 757–765.
[98] Lee, J., 2009, "Role of Surface Roughness in Water Spray Cooling Heat Transfer of Hot Steel Plate," ISIJ Int., **49**(12), pp. 1920–1925.
[99] Hsieh, S. S., Luo, S. Y., Lee, R. Y., and Liu, H. H., 2015, "Spray Cooling Heat Transfer on Microstructured Thin Film Enhanced Surfaces," Exp. Therm. Fluid Sci., **68**, pp. 123–134.
[100] Sehmbey, M. S., Pais, M. R., and Chow, L. C., 1992, "Effect of Surface Material Properties and Surface Characteristics in Evaporative Spray Cooling," J. Thermophys. Heat Transfer, **6**(3), pp. 505–512.
[101] Thiagarajan, S. J., Narumanchi, S., and Yang, R. G., 2014, "Effect of Flow Rate and Subcooling on Spray Heat Transfer on Microporous Copper Surfaces," Int. J. Heat Mass Transfer, **69**, pp. 493–505.
[102] Kim, J. H., You, S. M., and Choi, S. U. S., 2004, "Evaporative Spray Cooling of Plain and Microporous Coated Surfaces," Int. J. Heat Mass Transfer, **47**(14–16), pp. 3307–3315.
[103] Kim, Y. H., Choi, C., Lee, K. J., and Han, D., 2009, "Experimental Study of Spray Cooling Performance on Micro-Porous Coated Surfaces," Heat Mass Transfer, **45**(10), pp. 1285–1292.
[104] de Souza, A. G. U., and Barbosa, J. R., 2012, "Spray Cooling of Plain and Copper-Foam Enhanced Surfaces," Exp. Therm. Fluid Sci., **39**, pp. 198–206.
[105] de Souza, A. G. U., and Barbosa, J. R., 2013, "Experimental Evaluation of Spray Cooling of R-134a on Plain and Enhanced Surfaces," Int. J. Refrig., **36**(2), pp. 527–533.
[106] Wang, H., Wu, J. J., Yang, Q., Zhu, X., and Liao, Q., 2016, "Heat Transfer Enhancement of Ammonia Spray Cooling by Surface Modification," Int. J. Heat Mass Transfer, **101**, pp. 60–68.
[107] Bostanci, H., Altalidi, S. S., and Nasrazadani, S., 2018, "Two-Phase Spray Cooling With HFC-134a and HFO-1234yf on Practical Enhanced Surfaces," Appl. Therm. Eng., **131**, pp. 150–158.
[108] Silk, E. A., and Bracken, P., 2010, "Spray Cooling Heat Flux Performance Using POCO HTC Foam," J. Thermophys. Heat Transfer, **24**(1), pp. 157–164.
[109] Hsieh, C. C., and Yao, S. C., 2006, "Evaporative Heat Transfer Characteristics of a Water Spray on Micro-Structured Silicon Surfaces," Int. J. Heat Mass Transfer, **49**(5–6), pp. 962–974.
[110] Chien, L. H., Wu, T. L., and Lee, S. C., 2011, "A Study of Spray-Impingement Cooling on Smooth and Pin-Finned Surfaces Using FC-72," J. Enhanc. Heat Transfer, **18**(5), pp. 375–387.
[111] Zhang, Z., Jiang, P. X., Ouyang, X. L., Chen, J. N., and Christopher, D. M., 2014, "Experimental Investigation of Spray Cooling on Smooth and Micro-Structured Surfaces," Int. J. Heat Mass Transfer, **76**, pp. 366–375.
[112] Xu, R.-N., Cao, L., Wang, G.-Y., Chen, J.-N., and Jiang, P.-X., 2020, "Experimental Investigation of Closed Loop Spray Cooling With Micro- and Hybrid Micro-/Nano-Engineered Surfaces," Appl. Therm. Eng., **180**, p. 115697.
[113] Sodtke, C., and Stephan, P., 2007, "Spray Cooling on Micro Structured Surfaces," Int. J. Heat Mass Transfer, **50**(19–20), pp. 4089–4097.
[114] Horacek, B., Kiger, K. T., and Kim, J., 2005, "Single Nozzle Spray Cooling Heat Transfer Mechanisms," Int. J. Heat Mass Transfer, **48**(8), pp. 1425–1438.
[115] Horacek, B., Kim, J., and Kiger, K. T., 2004, "Spray Cooling Using Multiple Nozzles: Visualization and Wall Heat Transfer Measurements," IEEE Trans. Device Mater. Rehabil., **4**(4), pp. 614–625.
[116] Coursey, J. S., Kim, J. G., and Kiger, K. T., 2007, "Spray Cooling of High Aspect Ratio Open Microchannels," ASME J. Heat Transfer, **129**(8), pp. 1052–1059.
[117] Hou, Y., Tao, Y. J., and Huai, X. L., 2014, "The Effects of Micro-Structured Surfaces on Multi-Nozzle Spray Cooling," Appl. Therm. Eng., **62**(2), pp. 613–621.
[118] Yang, B. H., Wang, H., Zhu, X., Liao, Q., Ding, Y. D., and Chen, R., 2013, "Heat Transfer Enhancement of Spray Cooling With Ammonia by Microcavity Surfaces," Appl. Therm. Eng., **50**(1), pp. 245–250.
[119] Bostanci, H., Rini, D. P., Kizito, J. P., and Chow, L. C., 2009, "Spray Cooling With Ammonia on Microstructured Surfaces: Performance Enhancement and Hysteresis Effect," ASME J. Heat Transfer, **131**(7), p. 071401.
[120] Kim, S., Kim, H. D., Kim, H., Ahn, H. S., Jo, H., Kim, J., and Kim, M. H., 2010, "Effects of Nano-Fluid and Surfaces With Nano Structure on the Increase of CHF," Exp. Therm. Fluid Sci., **34**(4), pp. 487–495.
[121] Hendricks, T. J., Krishnan, S., Choi, C., Chang, C.-H., and Paul, B., 2010, "Enhancement of Pool-Boiling Heat Transfer Using Nanostructured Surfaces on Aluminum and Copper," Int. J. Heat Mass Transfer, **53**(15–16), pp. 3357–3365.

[122] Chen, R., Lu, M.-C., Srinivasan, V., Wang, Z., Cho, H. H., and Majumdar, A., 2009, "Nanowires for Enhanced Boiling Heat Transfer," Nano Lett., **9**(2), pp. 548–553.
[123] Zhang, Z., Jiang, P. X., Christopher, D. M., and Liang, X. G., 2015, "Experimental Investigation of Spray Cooling on Micro-, Nano- and Hybrid-Structured Surfaces," Int. J. Heat Mass Transfer, **80**, pp. 26–37.
[124] Zhou, Z. F., Lin, Y. K., Tang, H. L., Fang, Y., Chen, B., and Wang, Y. C., 2019, "Heat Transfer Enhancement Due to Surface Modification in the Close-Loop R410a Flash Evaporation Spray Cooling," Int. J. Heat Mass Transfer, **139**, pp. 1047–1055.
[125] Srikar, R., Gambaryan-Roisman, T., Steffes, C., Stephan, P., Tropea, C., and Yarin, A. L., 2009, "Nanofiber Coating of Surfaces for Intensification of Drop or Spray Impact Cooling," Int. J. Heat Mass Transfer, **52**(25–26), pp. 5814–5826.
[126] Fischer, S., Sahu, R. P., Sinha-Ray, S., Yarin, A. L., Gambaryan-Roisman, T., and Stephan, P., 2017, "Effect of Nano-Textured Heater Surfaces on Evaporation at a Single Meniscus," Int. J. Heat Mass Transfer, **108**, pp. 2444–2450.
[127] Weickgenannt, C. M., Zhang, Y. Y., Sinha-Ray, S., Roisman, I. V., Gambaryan-Roisman, T., Tropea, C., and Yarin, A. L., 2011, "Inverse-Leidenfrost Phenomenon on Nanofiber Mats on Hot Surfaces," Phys. Rev. E, **84**(3), p. 036310.
[128] Chen, X., Chen, J., Ouyang, X., Song, Y., Xu, R., and Jiang, P., 2017, "Water Droplet Spreading and Wicking on Nanostructured Surfaces," Langmuir, **33**(27), pp. 6701–6707.
[129] Alvarado, J. L., and Lin, Y.-P., 2011, "Multiple Droplet Impingements on Nanostructured Surfaces for Enhanced Spray Cooling," ASME Paper No. AJTEC2011-44509.
[130] Bostanci, H., Rini, D. P., Kizito, J. P., Singh, V., Seal, S., and Chow, L. C., 2012, "High Heat Flux Spray Cooling With Ammonia: Investigation of Enhanced Surfaces for CHF," Int. J. Heat Mass Transfer, **55**(13–14), pp. 3849–3856.
[131] Bostanci, H., Rini, D. P., Kizito, J. P., Singh, V., Seal, S., and Chow, L. C., 2014, "High Heat Flux Spray Cooling With Ammonia: Investigation of Enhanced Surfaces for HTC," Int. J. Heat Mass Transfer, **75**, pp. 718–725.
[132] Romashevskiy, S. A., and Ovchinnikov, A. V., 2018, "Functional Surfaces With Enhanced Heat Transfer for Spray Cooling Technology," High Temp., **56**(2), pp. 255–262.
[133] Tenzer, F. M., Roisman, I. V., and Tropea, C., 2019, "Fast Transient Spray Cooling of a Hot Thick Target," J. Fluid Mech., **881**, pp. 84–103.
[134] Zhao, T. Y., and Patankar, N. A., 2019, "The Thermo-Wetting Instability Driving Leidenfrost Film Collapse," PNAS, **117**(24), pp. 13321–13328.
[135] Shedd, T. A., 2007, "Next Generation Spray Cooling: High Heat Flux Management in Compact Spaces," Heat Transfer Eng., **28**(2), pp. 87–92.
[136] Toda, S., 1973, "A Study of Mist Cooling: 3rd Report, the Theory of Mist Cooling-Thermal Behaviors of Liquid Films Formed of Mist Drops on a Heated Surface at High Temperatures and High Heat Fluxes," Trans. Jpn. Soc. Mech. Eng., **39**(323), pp. 2172–2185.
[137] Chen, K., Xu, R.-N., and Jiang, P.-X., 2020, "Evaporation Enhancement of Microscale Droplet Impact on Micro/Nanostructured Surfaces," Langmuir, **36**(41), pp. 12230–12236.
[138] Chen, R. H., Tan, D. S., Lin, K. C., Chow, L. C., Griffin, A. R., and Rini, D. P., 2008, "Droplet and Bubble Dynamics in Saturated FC-72 Spray Cooling on a Smooth Surface," ASME J. Heat Transfer, **130**(10), p. 101501.
[139] Tsai, P. C. A., van der Veen, R., van de Raa, M., and Lohse, D., 2010, "How Micropatterns and Air Pressure Affect Splashing on Surfaces," Langmuir, **26**(20), pp. 16090–16095.
[140] Bouwhuis, W., van der Veen, R. C., Tran, T., Keij, D. L., Winkels, K. G., Peters, I. R., van der Meer, D., Sun, C., Snoeijer, J. H., and Lohse, D., 2012, "Maximal Air Bubble Entrainment at Liquid-Drop Impact," Phys. Rev. Lett., **109**(26), p. 264501.
[141] Tran, T., de Maleprade, H., Sun, C., and Lohse, D., 2013, "Air Entrainment During Impact of Droplets on Liquid Surfaces," J. Fluid Mech., **726**, R3.
[142] Chen, J. N., Zhang, Z., Xu, R. N., Ouyang, X. L., and Jiang, P. X., 2016, "Numerical Investigation of the Flow Dynamics and Evaporative Cooling of Water Droplets Impinging Onto Heated Surfaces: An Effective Approach to Identify Spray Cooling Mechanisms," Langmuir, **32**(36), pp. 9135–9155.
[143] Kunkelmann, C., Ibrahem, K., Schweizer, N., Herbert, S., Stephan, P., and Gambaryan-Roisman, T., 2012, "The Effect of Three-Phase Contact Line Speed on Local Evaporative Heat Transfer: Experimental and Numerical Investigations," Int. J. Heat Mass Transfer, **55**(7–8), pp. 1896–1904.
[144] Ibrahem, K., Abd Rabbo, M. F., Gambaryan-Roisman, T., and Stephan, P., 2010, "Experimental Investigation of Evaporative Heat Transfer Characteristics at the 3-Phase Contact Line," Exp. Therm. Fluid Sci., **34**(8), pp. 1036–1041.
[145] Wee, S.-K., 2004, "Microscale Observables for Heat and Mass Transport in Sub-Micron Scale Evaporating Thin Film," Ph.D. thesis, Texas A&M University, College Station, TX.
[146] Wemp, C. K., and Carey, V. P., 2017, "Water Wicking and Droplet Spreading on Randomly Structured Thin Nanoporous Layers," Langmuir, **33**(50), pp. 14513–14525.
[147] Quéré, D., 2008, "Wetting and Roughness," Annu. Rev. Mater. Res., **38**(1), pp. 71–99.
[148] Wemp, C. K., and Carey, V. P., 2018, "Tuning Superhydrophilic Nanostructured Surfaces to Maximize Water Droplet Evaporation Heat Transfer Performance," ASME J. Heat Transfer, **140**(10), p. 102401.
[149] Gregorčič, P., Zupančič, M., and Golobič, I., 2018, "Scalable Surface Microstructuring by a Fiber Laser for Controlled Nucleate Boiling Performance of High-and Low-Surface-Tension Fluids," Sci. Rep. Uk, **8**(1), pp. 1–8.
[150] Wen, R., Xu, S., Zhao, D., Yang, L., Ma, X., Liu, W., Lee, Y.-C., and Yang, R., 2018, "Sustaining Enhanced Condensation on Hierarchical Mesh-Covered Surfaces," Natl. Sci. Rev., **5**(6), pp. 878–887.
[151] Li, T., Liu, H., Zhao, X., Chen, G., Dai, J., Pastel, G., Jia, C., Chen, C., Hitz, E., Siddhartha, D., Yang, R., and Hu, L., 2018, "Scalable and Highly Efficient Mesoporous Wood-Based Solar Steam Generation Device: Localized Heat, Rapid Water Transport," Adv. Funct. Mater., **28**(16), p. 1707134.
[152] He, W., Luo, Z., Deng, X., and Xia, Z., 2020, "A Novel Spray Cooling Device Based on a Dual Synthetic Jet Actuator Integrated With a Piezoelectric Atomizer," Heat Mass Transfer, **56**(5), pp. 1551–1563.
[153] van Erp, R., Soleimanzadeh, R., Nela, L., Kampitsis, G., and Matioli, E., 2020, "Co-Designing Electronics With Microfluidics for More Sustainable Cooling," Nature, **585**(7824), pp. 211–216.
[154] Yata, V. V. R., and Bostanci, H., 2017, "Investigation of Spray Cooling Schemes for Dynamic Thermal Management," 16th IEEE Intersociety Conference on Thermal and Thermomechanical Phenomena in Electronic Systems (ITherm), Orlando, FL, May 30–June 2, pp. 744–751.
[155] Tsang, S., and Sun, C-L., 2020, "Utilizing the Inverse Marangoni Convection to Facilitate Extremely-Low-Flow-Rate Intermittent Spray Cooling for Large-Area Systems," Appl. Therm. Eng., **166**, p. 114725.
[156] Jiang, P.-X., Huang, G., Zhu, Y., Xu, R., Liao, Z., and Lu, T., 2017, "Experimental Investigation of Biomimetic Self-Pumping and Self-Adaptive Transpiration Cooling," Bioinspirat. Biomimet., **12**(5), p. 056002.
[157] Huang, G., Zhu, Y., Liao, Z., Xu, R., and Jiang, P.-X., 2019, "Biomimetic Self-Pumping Transpiration Cooling for Additive Manufactured Porous Module With Tree-Like Micro-Channel," Int. J. Heat Mass Transfer, **131**, pp. 403–410.